1 **Mapping textures of polar ice cores using 3D laboratory X-ray microscopy**

2

3 Olivia A. Barbee[1,2], Jette Oddershede[2], Ravi Raj Purohit Purushottam Raj Purohit[2], Håkon W.

4 Ånes[2], Jonas Engqvist[1], Anders Svensson[3], Nicholas M. Rathmann[3], Thomas Blunier[3], Florian

5 Bachmann[2], and Stephen Hall[1]

6

7 [1]Division of Solid Mechanics, Lund University, Lund, Sweden

8 [2]Xnovo Technology ApS, Køge, Denmark

9 [3]Physics of Ice, Climate and Earth, Niels Bohr Institute, University of Copenhagen, Copenhagen, Denmark

10 Corresponding author: Olivia A. Barbee (oliviaabarbee@gmail.com)

11

12 **ABSTRACT**

13 Deep ice cores from polar ice sheets enable reconstructions of Earth's past climate. Ice-core

14 records are therefore crucial for projecting future climate change, however, our ability to

15 interpret them relies on our understanding of polycrystalline-ice microstructures and

16 mechanics. In turn, these microstructures enable modeling of ice flow and large-scale effects of

17 ice-sheet evolution. Since drilling began in the 1950s, the ice textures and climate proxies

18 developed to decipher ice-core records have been analyzed in one- or two-dimensional (2D)

19 spaces, necessitated by the analytical instruments of core-processing lines and laboratories.

20 Here we develop a three-dimensional (3D), non-destructive approach to textural analysis that

21 preserves the natural context of ice and complements standard methods. Our method

22 combines lab-based absorption and diffraction contrast tomography to simultaneously

23 visualize, measure, and spatially correlate ice grains and air bubbles from volumetric and 3D

24 crystallographic perspectives, both lost during traditional sample preparations. We evaluate the

25 representation of 3D versus 2D data and discuss how access to both c- and a-axis directions of

26 grains may help constrain micromechanical models. We also built a specially designed cooling

27 device for the laboratory X-ray system to extend observational volumes by several orders of

28 magnitude over previous synchrotron-based measurements.

29

1 INTRODUCTION

30

31   Continental ice sheets covering Greenland and Antarctica play pivotal roles in Earth's

32 climate system. Deep drill cores of these ice sheets reveal they have captured and preserved

33 their response to past climates continuously over the last one hundred thousand to one million

34 years, providing a means to reconstruct the past to help predict future climate and project

35 changes in ice-sheet mass, geometry, and sea-level (e.g., Faria and others, 2014; Lauritzen and

36 others, 2024). Reconstructions of climate records and ice dynamics use the same archive of ice-

37 core layers and are interdependent in many ways. That is, when these layers formed through

38 the burial and compaction of recurrent snowfalls, they trapped ancient atmospheres in the

39 form of air bubbles, airborne particles, and elemental and isotopic abundances, but interpreting

40 their stratigraphic chronology relies on our understanding of ice-grain mechanics and

41 interactions with these climate proxies (e.g., Faria and others, 2010; NEEM community

42 members, 2013; Faria and others, 2014; Westhoff and others, 2021). More specifically, how

43 microstructural mechanisms facilitate the creeping flow of ice sheets at the crystal-scale not

44 only informs the origin and integrity of ice-core stratigraphy but also allows large-scale ice-

45 sheet evolution and its climatic effects to be modeled (Fan and Prior, 2023; Gerber and others,

46 2023; Zhang and others, 2024). Our ability to interpret such information, however,

47 fundamentally relies on our approach to textural analysis (grain and bubble morphologies,

48 sizes, orientations) and how we access ice layers to begin with.

49   Since polar ice core drilling began in the 1950s, scientists have accessed thousands of

50 meters of ice-sheet stratigraphy by developing what are now standard core-processing

51 techniques. These include an assembly line of instruments and saws to measure along-core

52 properties and to send samples to various labs for gas, chemistry, and isotope analysis.

53 Although traditional sample preparations and analytical techniques involve dissection of the ice

54 cores and can remove important three-dimensional (3D) context (Westhoff and others, 2021;

55 Disbrow-Monz and others, 2024), one- and two-dimensional (2D) analyses have led to detailed

56 climate-record reconstructions and form the basis of most textural studies carried out to date

57 (e.g., Svensson, Baadsager, and others, 2003; Durand and others, 2006; Binder and others,

58 2013; Montagnat, Azuma, and others, 2014; Fan and others, 2021; Stoll and others, 2024). A

59 question remains, however, as to what scientists can learn if they initially and routinely have

60 access to ice-core textures in 3D.

61   Progress towards 3D characterization of snow and ice textures has been made over the

62 last two decades using X-ray microtomography. Air bubbles in deep ice cores are often

63 relatively easy to wholly visualize by X-ray attenuation given their small scale and low density

64 compared to ice grains, making it possible to measure porosity and contextualize trapped

65 greenhouse gases (Burr and others, 2018; Baker, 2019). However, in both synchrotron- and lab-

66 based X-ray systems, challenges surrounding the necessary cold analytical environments and

67 sample-size limitations mean that sufficient grain numbers with crystal orientation

68 measurements have not been achieved (e.g., Flin and others, 2004; Schneebeli and Sokratov,

69 2004; Kaempfer and Schneebeli, 2007; Rolland du Roscoat and others, 2011; Heggli and others,

70 2011; Riche and others, 2013; Granger and others, 2021).

71   However, crystal orientations are thought to play a critical role in ice-sheet evolution,

72 which begins with the intrinsic visco-plastic anisotropy of each ice crystal's hexagonal structure

73 (Fan and others, 2021; Fan and Prior, 2023). The basal plane in ice has a relatively low

74 resistance to shear, thus the gravity-driven flow occurring in ice sheets causes dislocation slip

75 mainly along the basal plane, while the crystal *c*-axis tends toward the compressive-stress

76 direction (Gow and Williamson, 1976; Alley, 1992). This leads to a bulk anisotropy manifesting

77 in crystallographic fabrics that develop under continued snow deposition, burial, and ice

78 deformation (Gow and Williamson, 1976). In effect, feedback occurs between fabrics and flow,

79 such that crystal orientations control the bulk mechanical behavior of the polycrystalline ice,

80 but the fabrics also evolve to conform to increased mechanical loading. Therefore, crystal

81 orientations exert an important rheological control on the large-scale flow of ice sheets (Duval

82 and others, 1983; Shoji and Langway, 1985; Gerber and others, 2023).

83   Depending on the extent and mechanisms of ice deformation, the *c*-axis fabric and

84 mechanical anisotropy of the ice layers can vary and evolve considerably over the depth of the

85 ice column (Faria and others, 2014). For this reason, crystal orientation measurements are

86 routinely performed with automatic fabric analyzers (AFAs) or other mapping methods that rely

87 on optical microscopy and cm-scale, 2D thin sections of ice cores (Wilson and others, 2003;

88   Kipfstuhl and others, 2006). Although these are high-resolution methods and can rapidly

89   measure *c*-axis directions for hundreds of grains, they cannot determine directions of the three

90   *a*-axes for each grain (Wilen and others, 2003; Wilson and others, 2014). This leaves

91   consequential gaps in textural data, such as whether grains are truly distinct from one another

92   outside the section plane (Disbrow-Monz and others, 2024), or whether *a*-axis directions can or

93   should be used as strain markers to understand ice flow (Lilien and others, 2023). Furthermore,

94   an incomplete understanding of how to parameterize the elastic and visco-plastic anisotropies

95   of individual grains partly prevents ice-flow models from accounting for their effects, at least to

96   the desired accuracy (Ranganathan and others, 2021; Richards and others, 2021; Lilien and

97   others, 2023; Ranganathan and Minchew, 2024). At present, coupling small-scale

98   micromechanical models with large-scale ice-flow models is rarely considered for two main

99   reasons. First, it has proven challenging to incorporate realistic, yet efficient, representations of

100   crystal fabrics into large-scale models (e.g., Montagnat, Castelnau, and others, 2014; Lilien and

101   others, 2023). Second, only a few ways have been proposed to parameterize the predictions

102   made by micromechanical models, each with their own caveats and limitations (Placidi and

103   others, 2010; Gillet-Chaulet and others, 2005).

104   In addition to crystal-orientation fabrics, more work is needed to understand the

105   influence of grain sizes, shapes, boundaries, and even bubbles on ice metamorphosis and how

106   they should also be parameterized in models (Kuiper and others, 2020). However, collecting

107   this microstructural information has proven challenging for polycrystalline ice. Optical and cryo-

108   electron backscatter diffraction (EBSD) techniques provide visibility of ice-grain boundaries, but

109   only in 2D (Prior and others, 2015). Whereas, X-ray tomography provides 3D context but

110   traditionally necessitates X-ray diffraction from mm-scale samples to distinguish individual

111   grains (Baker, 2019). Ultimately, gaining the ability to correlate 3D behaviors of microstructures

112   and bubbles in ice cores over large sample volumes could improve both paleoclimate

113   reconstructions and the physical realism of large-scale ice-flow models.

114   Here we present a new non-destructive 3D method for textural analysis that

115   complements standard methods used in ice-core studies. Our method makes it possible to

116   simultaneously map ice grains and pore spaces in 3D, while measuring their volumes and

117   shapes with respect to complete crystallographic orientations of the grains. The method

118   combines two lab-based X-ray modalities—absorption (ACT) and diffraction contrast

119   tomography (DCT)—which enable the visualization, measurement, and spatial correlation of

120   ice-grain and air-bubble textures, adding new perspectives on ice-core stratigraphy and new

121   ways to access modeling parameters. We achieve this by pushing the spatial resolution and

122   sample volume limits of DCT in the lab and by mitigating challenges in X-ray diffraction posed

123   by crystal deformation. Our measurement approach is based upon a specially designed cooling

124   device that accommodates ~3 x 3 x 3 cm^3 samples containing hundreds to thousands of grains,

125   extending observational volumes of ice by one to four orders of magnitude over those quoted 5

126   to 30 years ago (e.g., Liu and others, 1992, 1995; Rolland du Roscoat and others, 2011; Baker,

127   2019). To demonstrate the power of greater spatial and statistical information, we evaluate the

128   representation of grain size distributions and orientations in 3D versus 2D, investigate grain and

129   bubble relationships in 3D, and discuss the relevance of complete 3D crystallographic

130   information in constraining micromechanical models that underpin current large-scale ice-flow

131   models.

132

133   **2 METHODS**

134   **2.1 Building a freezer inside the laboratory X-ray microscope**

135   A cooling device was designed at Lund University under the requirement that it (1)

136   keeps ice at a temperature well below -10°C and (2) maximizes sample size while minimizing

137   grain diffraction overlap, which we simulated beforehand. A sketch of the experimental set-up

138   is shown in **Figure 1**. Each sample sat directly on a 34 mm-diameter aluminum plate that was

139   cooled by a Peltier element. The hot bottom-side of the Peltier was kept cold using an external

140   chiller, attached to the device through an integrated slip ring system that held fluid hoses

141   stationary during sample rotation. Sample housing above the plate included a 27 mm-tall

142   polymer (PMMA) tube with 3 mm-thick walls, as well as surrounding polyethylene foam with 13

143   mm-thick walls, bringing the total housing diameter to 66 mm. For 30 minutes, chiller fluid

144   cooling to 5°C was circulated through the device before powering the Peltier and setting it to -

145   35°C, an unobtainable target that prevented temperature regulation. Plate sensor readings

146   reached -29°C in 10 minutes and remained stable below each sample during data acquisition

147   (up to 24 hours). A sensor embedded 3 mm beneath the upper sample surface also read stable

148   at -21°C during a test. While not ideal, thermal gradients of ~0.3°C/mm across the ~3 cm

149   sample height had negligible effects on ice microstructures at these temperatures and on our

150   analytical timescales. Air temperatures between the upper sample surface and insulating foam

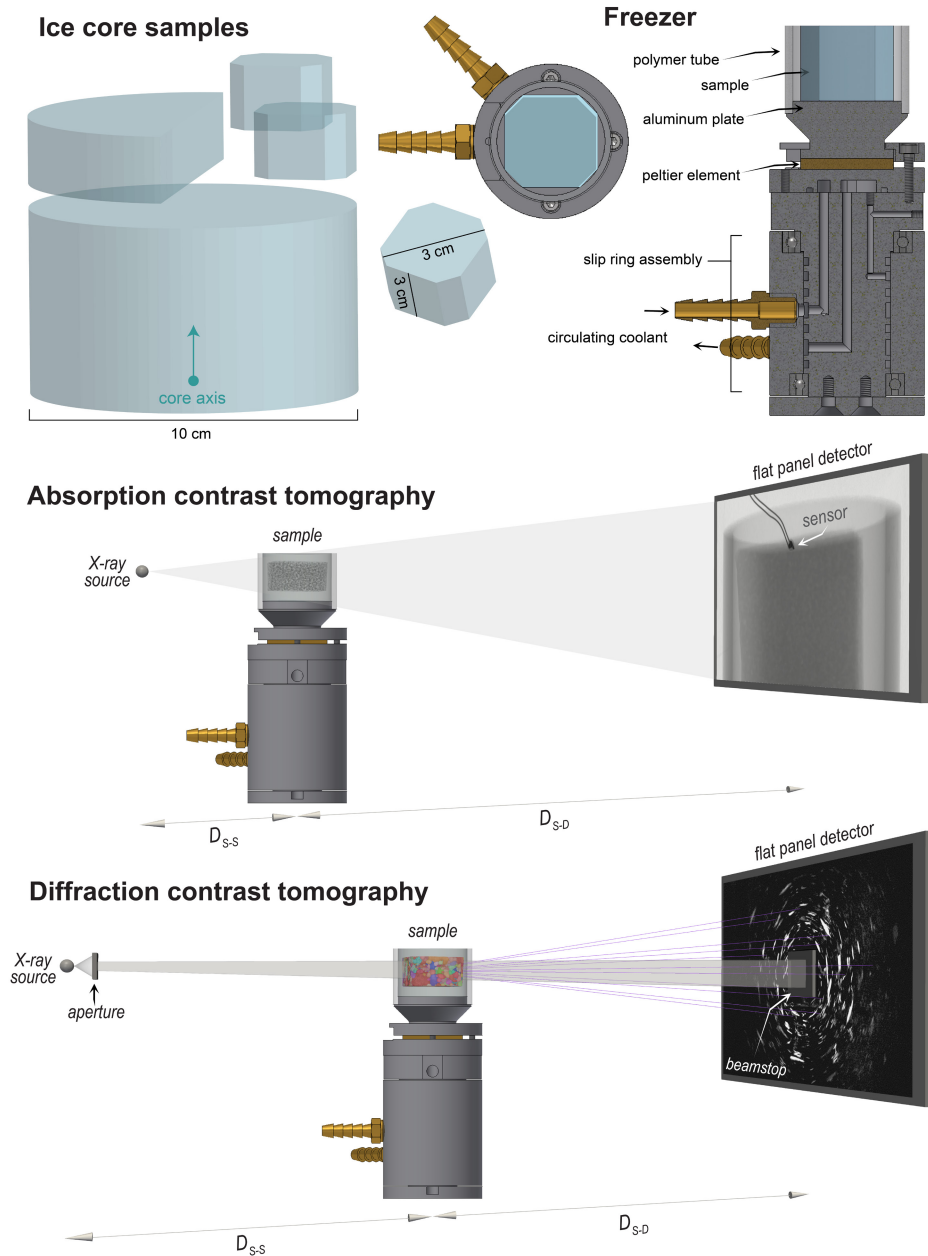151   reached -14°C in 5-7 minutes and typically continued to decrease by a few degrees.

152

153   **Figure 1.** The cooling device, sample and beam geometries used for lab-based multimodal X-ray imaging.

154   Examples of absorption and diffraction contrast projection data shown here correspond to a subvolume

155 of a firn sample described in Section 2.2. Source-to-sample and sample-to-detector distances are

156 referred to as D_{S-S} and D_{S-D}, respectively, and are provided in Section 2.3.

157

2.2 Selecting and working with ice core samples

159 We selected 10 samples from the Niels Bohr Institute's ice-core archive at the University

160 of Copenhagen. Samples include firn and Holocene-age deep ice from central, northwestern,

161 and southern drilling sites on Greenland (i.e., EGRIP, Eurocore, NEEM, and Dye-3; **Fig. 2**). For

162 experimental purposes, we targeted non-precious cores that had suffered drilling and recovery

163 complications in the field. Of the samples, we focused on three that cover a range in depth and

164 enabled us to develop methods and establish proof-of-concept (**Fig. 2**; **Table 1**). Each sample

165 captures less than one year, and in some cases less than one winter or summer season, based

166 on its thickness (0.03 m) and the annual ice-layer thickness at the depth it was extracted from.

167 The original cores have been stored at -30°C for durations that can be deduced from their

168 drilling dates in **Table 1**.

169 Sections of the 10 cm-diameter cores were sawn inside a walk-in freezer at the

170 University of Copenhagen and cut into smaller, ~3 x 3 x 3 cm^3 samples (**Fig. 1**). The samples

171 were then sealed in plastic bags and transported for 1 hour by cooler box to Xnovo Technology

172 in Køge, Denmark for X-ray imaging. The cooler box and its contents were stored for a few days

173 to months between -20 and -25°C inside a small, temperature-monitored freezer next to the X-

174 ray microscope. Ice exposure to room temperature lasted 2-4 seconds when samples were

175 transported by cold steel tweezers into the X-ray microscope cabinet. Mounted samples were

176 frozen to the aluminum plate using one drop of water, which temporarily increased the plate

177 temperature by 1°C. No ice metamorphosis occurred before or during data acquisition,

178 although an inconsequential <2 mm layer of frost commonly accumulated on sample surfaces

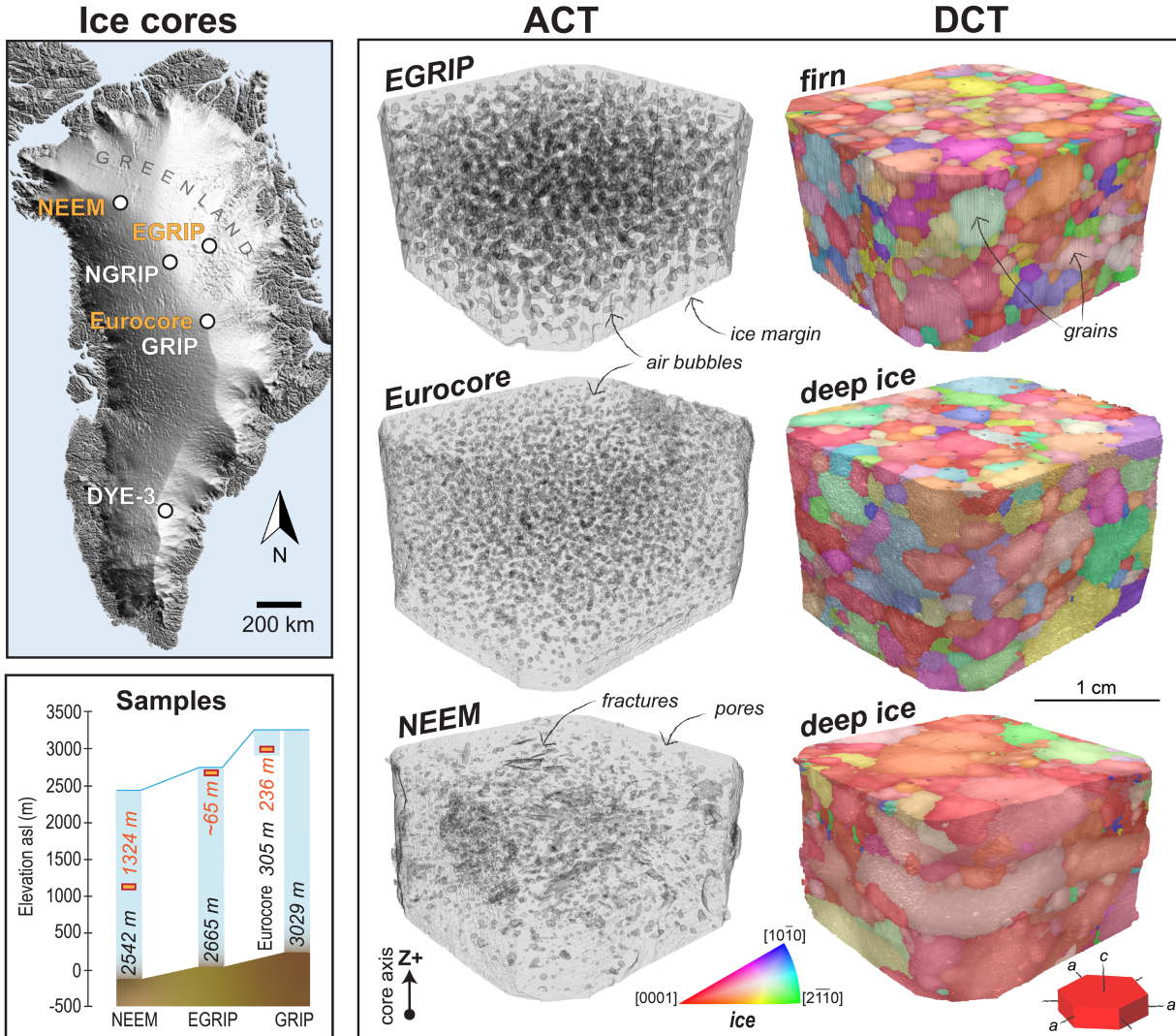179 while inside the cooling device.

180

181

Figure 2. Overview of the three ice-core sample datasets used for method development. We screened samples from five ice-core drilling sites shown on the DEM of Greenland. In this paper, we present sample data from the sites labeled in orange (also see **Table 1**). Sample depths are provided with elevations and the final core depths at those drilling sites. EastGRIP was drilled between 2016 and 2023 within the active Northeast Greenland Ice Stream (NEGIS). The depth of the EGRIP firn sample is estimated based on sample porosity and firn density profiles of NEGIS (Vallelonga and others, 2014). Eurocore was drilled in 1989, just 30 m away from the GRIP site (GReenland Ice core Project, drilled 1990-92). Our deepest sample is from the NEEM core (North Greenland Eemian ice drilling project), drilled between 2009 and 2012. The observed differences in porosity and grain sizes between the three samples generally reflect their different depths within the ice sheet.

Table 1. Details of Holocene samples from Greenland ice cores

Sample	Core site	Year drilled	Depth (m)	Date[a-c]	Age (ka)	Annual layer thickness (m/yr)[a-c]
Firn	EGRIP	2016	~65	~1620 CE	~0.4	0.12
Late Holocene	Eurocore (GRIP)	1989	236	~1030 CE	~1.0	0.25
Early Holocene	NEEM	2010	1324	~7610 BCE	~9.6	0.06

[a]Mojtabavi and others (2020); [b]Seierstad and others (2014); [c]Rasmussen and others (2013)

194

195   ## 2.3 Absorption and diffraction contrast tomography

196   Ice textures were characterized through correlative, multimodal X-ray imaging using a

197   Zeiss Xradia 520 Versa X-ray microscope equipped with a LabDCT Pro module. Absorption

198   contrast tomography was used to visualize sample morphology and determine the shapes of

199   pore spaces, including trapped (primary) air bubbles and secondary pores and fractures.

200   Whereas, diffraction contrast tomography was used to measure and map 3D crystallographic

201   orientations and shapes of grains. Grains can only be defined by DCT, because they lack

202   contrast in ACT due to their same composition and density. The crystal lattice distortion

203   inherent to glacial processes prompted us to explore different X-ray scanning conditions to

204   optimize data collection from grains that are plastically deformed, a general challenge in X-ray

205   diffraction methods (**Figure S1**).

206   To optimize absorption contrast between ice and pore spaces, ACT scans were

207   performed at 80 kV and 7 W. We placed the X-ray source at 61 mm and detector at 245 mm

208   away from the sample to maximize spatial resolution while avoiding hardware collision with the

209   cooling device (**Fig. 1**). These distances created a geometrical magnification of 5x that

210   corresponded to a large, roughly 46 x 29 mm^2 field of view on the flat panel detector, which, as

211   a result, produced a tomography image containing 3064 x 1936 pixels at a nominal size of 75

212   μm and effective size of 14.95 μm. We collected 3201 projections (images), each with 0.5

213 seconds of exposure, as the sample completed a 360° rotation. This ACT acquisition step took

214 less than 2 hours.

215   Directly after the ACT scan, we performed the correlative DCT scan. Given that many

216 grains lie in the X-ray beam's path, we optimized diffraction patterns for crystallographic

217 reconstruction by performing DCT scans (110 kV, 10 W) with the flat panel detector in a

218 projection geometry close to Laue focusing (Bachmann and others, 2019), such that source-to-

219 sample (200 mm) and sample-to-detector (245 mm) distances were similar enough to produce

220 radially-focused, linear diffraction spots that reduced spot overlap (**Fig. 1**). Two different

221 source-beam apertures were used depending on the extent of grain deformation, which causes

222 a radial spread of cloudy and elongated diffraction spots, known as asterism (**Figure S1**). A 375 x

223 375 μm^2 square aperture was used for firn and deep ice from <300 m depths. Whereas, a 200

224 μm circular pinhole aperture improved results for much deeper (1000s of meters) and more

225 deformed ice by (1) illuminating less sample volume per projection and (2) improving

226 diffraction spot definition by constraining spots to the aperture's pinhole shape. Depending on

227 the aperture used, our source distance gave roughly a 9 x 9 mm^2 to 5 x 5 mm^2 field of view. To

228 keep experiment times to a day, partial sample volumes of approximately 3 x 3 x 1.7 cm^3 were

229 covered in one advanced helical phyllotaxis raster scan (Oddershede and others, 2022)

230 consisting of 1119 to 5061 projections, each with an exposure time of either 5 or 10 seconds for

231 the larger aperture and 10 seconds for the pinhole. The DCT acquisition step took

232 approximately 5-6 hours when using the larger aperture and 20 hours using the pinhole. From

233 start to finish, each multimodal imaging measurement was completed in ~8-24 hours.

234

235 **2.4 Data reconstruction and processing**

236 *2.4.1 Ice and pore volumes*

237   We reconstructed sample volumes from the ACT data using cubic voxels with side-

238 lengths of 14.95 μm. This was performed using a filtered back projection routine and the

239 reconstructor tool in ZEISS Scout-and-Scan software. Because individual ice grains have the

240 same density, they cannot be distinguished by way of X-ray attenuation and thus form one

241 continuous volume with homogenous grayscale intensity. Much lower density air bubbles >40

242 μm in diameter and apparent microfractures were detectable at the reconstructed voxel size,

243 while dust impurities, which are typically on the order of a few micrometers, fell below the

244 detection limit.

245

246 *2.4.2 Ice grain crystallographic orientations and morphologies*

247 Using Xnovo Technology's GrainMapper3D software, crystallographic maps were

248 reconstructed from the DCT data with 60 μm-wide cubic voxels inside the volume mask

249 obtained from the ACT data (Bachmann and others, 2019; **Fig. 2**). Natural ice on Earth occurs as

250 ice Ih (ice one hexagonal), which belongs to the hexagonal crystal system and dihexagonal

251 dipyramidal 6/*mmm* Laue class (and point group). Lattice parameters for space group $P6_3/mmc$

252 of a = 4.489 Å, c = 7.327 Å and the four {*hkil*} families {$2\overline{1}\overline{1}0$}, {$10\overline{1}0$}, {$10\overline{1}3$}, and {$2\overline{1}\overline{1}2$} were

253 used to reconstruct ice grains from diffraction patterns. We use **Figure 3** to show how we

254 define grains and subgrains in our data. Adjacent regions in 3D space were assigned to the

255 same "grain" if the voxel-to-voxel, crystallographic angular misorientation was <2° (EGRIP firn,

256 Eurocore deep ice) or <3° (NEEM deep ice). Lower misorientation thresholds yielded large

257 numbers of low confidence grains a few hundred microns in size, which were interpreted to be

258 unphysical. Therefore, grain maps were cleaned by replacing any grain with a neighboring grain

259 that it shared the largest boundary area with, based on fulfillment of at least two of the

260 following three criteria indicative of poor reconstruction: (1) a mean completeness of <60%

261 across the grain (completeness is defined as the ratio between the number of observed and

262 expected diffraction spots for a given orientation); (2) a grain volume less than 8^3 = 512 voxels

263 (equivalent sphere diameter <600 μm); (3) a misorientation to a neighbor-of-a-neighbor grain

264 of <2° (EGRIP firn, Eurocore deep ice) or <4° (NEEM deep ice).

265 We calculated crystallographic misorientations using the difference between a

266 reconstructed grain's average orientation and the orientations of individual voxels composing

267 that grain (i.e., the grain reference orientation deviation). Because we considered adjacent

268 voxels with <2-3° misorientations to be the same "grain", the maximum misorientations of

269 subgrains with low-angle grain boundaries were defined to be <2° or <3°, depending on the

270 specific sample. However, different misorientation thresholds can be tested to define grains

271 and subgrains, depending on the scientific question of interest. We show in **Figure 3** that

272 combined maps of completeness, inverse pole figures (IPFs), and grain reference orientation

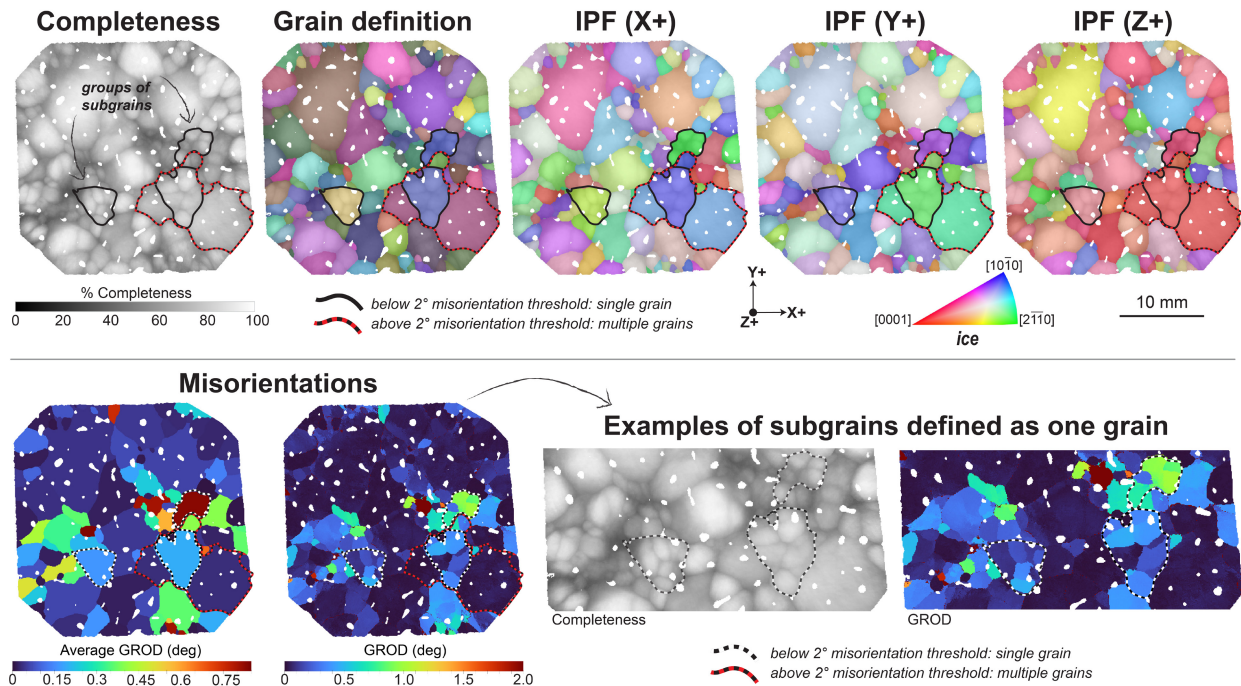273 deviations (GRODs) can be used to characterize subgrains.

274

275

Figure 3. Grain and subgrain definition in this study. Grains were reconstructed based on our chosen

277 scanning conditions and crystallographic misorientation thresholds described in the **Methods**. Virtual

278 slices of 3D grain maps of the EGRIP firn sample are used here for demonstrative purposes, wherein we

279 defined grains based on a 2° misorientation threshold. Grain completeness typically drops both at grain

280 and subgrain boundaries, enabling their visualization. This is because of the 1:1 relationship between

281 the shapes of diffraction spots on the detector and the shapes of the diffracting volumes (i.e., grains or

282 subgrains), with the spot edges corresponding to grain and subgrain boundaries. As a note, the

283 completeness map underlies all other maps shown in the top row. The grain definition map reflects our

284 chosen misorientation threshold to define grains, resulting in groupings of adjacent regions defined by

285 completeness drop-off and circled in black. When looking at IPF maps for XYZ directions, regions defined

286 as one grain appear with the same IPF color, consistent with the grain definition map. IPF coloring may

287 be similar for neighboring grains above the chosen misorientation threshold, such as those circled by

288 red-dashed lines. The grain reference orientation deviation (GROD) maps verify that apparent subgrains

289   identified in previous maps can be interpreted as such, given that the locations of completeness drop-

290   off correspond to low-angle misorientation boundaries.

291

292   **2.5 Data analysis and visualization**

293   Our analysis was focused on demonstrating the complementarity of 3D and 2D data, as

294   well as the new possibilities offered by 3D data available through our method. Therefore, the

295   analysis is limited in scope regarding ice mechanics and climate records. We instead focus on

296   comparing traditional and new perspectives using a few of the most common types of texture

297   analyses performed on ice cores. All analyses and 3D visualizations were generated using in-

298   house code at Xnovo Technology, GrainMapper3D (Bachmann and others, 2019), Paraview

299   (Ayachit, 2015), or the Python package Vedo (Musy and others, 2025).

300

301   *2.5.1 Grain sizes*

302   Grain size statistics were derived from both 3D reconstructed volumes and 2D cross-

303   sectional slices for comparison. Two grain metrics, the equivalent grain diameter and major-axis

304   length, were chosen to demonstrate the comparisons in **Figures 4 and 5** (also see **Fig. S2**). For

305   each grain and each slicing axis (X, Y, Z), the mean, minimum, and maximum values of the

306   chosen 2D metric across all slices intersecting that grain were calculated. In the generated

307   scatter plots, each point represents a single grain, with the 3D metric value compared to the

308   mean 2D metric value calculated from all slices intersecting the grain, either along a specified

309   slicing axis or XYZ axes combined. Vertical bars were added to each point (grain) to indicate the

310   minimum and maximum 2D metric value observed when slicing along a specified axis.

311   Additionally, grain size distributions based on the equivalent diameter were visualized through

312   histograms that emphasize the contribution of different sizes to the total volume (for 3D) or

313   total area (for 2D slices). For demonstrative purposes, grain-related analyses include grains that

314   intersect the sample margins due the presence of larger grain sizes (cf. Svensson, Baadsager,

315   and others, 2003).

316

2.5.2 Grain orientations

Pole figure analysis involved plotting separately: (1) the number-weighted grain orientations; (2) the volume-weighted grain orientations; and (3) all grains compared to those of separate grain size fractions for (1) and (2) (**Figs. 6 and 7**). To do this, we plotted and symmetrized discrete *c*-axis and *a*-axes directions for each grain within the sample reference frame (XYZ). The kernel density of the distribution of crystal axis directions was estimated using a de La Vallee Poussin kernel with a halfwidth (kappa) of 10°, and weighting them by number or volume. A unit sphere grid with density weights was plotted in a filled tri-contour plot in an equal-angle, lower-hemisphere stereographic projection.

2.5.3 Pore positions and shapes

Pore analysis in 3D leveraged complementary information from ACT and DCT datasets. To gain insight into spatial relationships between pores and grains, we correlated ACT segmentation and DCT grain labels. After segmenting pores from the ACT volume, a connected components analysis was used to identify individual pores and calculate their voxel count, volume, equivalent sphere diameter, and centroid. Pore-grain adjacency was then determined relative to the DCT grain map, such that the neighborhood of each identified ACT pore was examined within the corresponding region of the DCT volume. The pore-grain adjacency was visualized by generating a surface mesh of grains in the DCT volume (colored by IPF crystallographic orientations) and overlaying it with the ACT-derived pore mesh (one color, gray), which made pore and grain boundary surfaces visible. These surfaces provided a visualization of ACT pores colored by the IPF orientation of their host grain(s). We then characterized pores based on their *position* and size with respect to grain boundaries, classifying them as "intragranular" or "intergranular" based on the number of unique adjacent DCT grain labels. Counts and sizes of total, intragranular, and intergranular pores were analyzed statistically. Pores that intersect sample margins had a negligible effect on the analytical results.

To characterize each pore based on its *shape* and size, we made principal measurements using ACT data and performed a convex hull fitting with a "minimum volume enclosing ellipsoid" containing a set of points. Fitted axis measurements were made for

346   ellipsoids following the axis convention $a \geq b \geq c$ [where ellipsoid factor, $EF = c/b - b/a$, and the

347   aspect ratio is a/c]. These measurements include axis length (L) and corresponding azimuth (φ)

348   and elevation (θ) after rotation. Analyses focused on measuring the extent and direction of

349   pore flattening or elongation with respect to the host grain's *c*-axis direction, as well as the

350   sample compression axis (Z), which is parallel to the ice-core axis. Only intragranular pores were

351   considered for the purpose of comparing results to those of Fegyveresi and others (2019), who

352   focused on intragrain deformation. Therefore, the intergranular pores touching grain

353   boundaries were excluded entirely from our shape-related analyses, while the intragranular

354   pores were also filtered to exclude those intersected by sample margins.

355

356   **3 RESULTS AND DISCUSSION**

357   **3.1 Visualizing ice grains and pores through correlative 3D images**

358   Herein we demonstrate some of the utility of lab-based, multimodal (ACT + DCT) X-ray

359   tomography for the 3D analysis of ice cores. For brevity, we focus on one firn sample and two

360   deep ice samples that cover a range in depth and metamorphosis, as exemplified by differences

361   in their porosities, grain sizes, shapes, and crystallographic orientations visible in **Figure 2**.

362   Again, reconstructing and correlating images of these parameters required the consecutive

363   collection of X-ray absorption and diffraction image data. When correlating the two image

364   types, pores and ice grains are numerable and their spatial characteristics and relationships

365   measurable in 3D. Notably, the correlated images enable fast qualitative assessments of ice

366   core textures that can guide and contextualize measurements.

367   Prior to any quantitative analysis, there is visible evidence of crystallographic preferred

368   orientations (CPOs) in the IPF maps in **Figure 2**. These maps are colored with respect to the

369   "up" or vertical (Z+) direction of ice cores, perpendicular to the glacier surface. The dominance

370   of red indicates a *c*-axis preferred orientation, such that many grains are oriented with the axis

371   near-vertical. These observations match those commonly made from automatic fabric analyzer

372   images of thin sections (e.g., Faria and others, 2014). The correlative maps also allow

373   qualitative observations of *a*-axis CPOs, as well as volumetric differences in porosity and grain

374   sizes between different samples.

375   For the samples we considered and the ~12-15 cm^3 volumes we correlated, we observed

376   representative air bubble sizes, shapes, and distributions, but capturing representative grain

377   sizes was challenging, as large grains can intersect sample margins or extend beyond imaged

378   volumes. Our observations are corroborated by previous documentations of bubbles, which

379   reach just tens of micrometers to millimeters beneath the lower part of the firn-column, where

380   bubbles become closed-off (e.g., Bendel and others, 2013; Westhoff and others, 2024). In

381   contrast, ice grains can reach centimeters at depth and even meters near warm bedrock (Baker,

382   2019). While we achieve a total sample size of ~3 cm tall x ~3 cm diameter, which is much

383   greater than sizes attempted previously in synchrotron- and lab-based multimodal experiments

384   (e.g., 2 mm thick up to 1 x 1 cm; Liu and others, 1992, 1995; Jia and others, 1996; Rolland du

385   Roscoat and others, 2011), we acknowledge that even larger samples would be ideal for

386   accurate characterizations of coarse-grained ice. However, larger samples equate to

387   measurement limitations, ranging from too many diffracting grains crowding the X-ray

388   detector, to resolution limits and long acquisition times.

389   Analyzing ice cores with grain sizes too large to capture whole is a problem for all

390   existing methods. When using optical microscopy and thin sections, the problem may be

391   compounded by irregular grain shapes, such that duplicated measurements of grains appearing

392   more than once in the section will influence CPO analysis (Svensson, Schmidt, and others, 2003;

393   Monz and others, 2021). Furthermore, although cryo-EBSD has been applied to serial sections

394   of coarse-grained ice to identify representative volumes, shapes, and sufficient grain numbers

395   needed for accurate CPO characterizations, this is labor-intensive and can create positional and

396   angular uncertainties when recombining sections and stitching data together (Monz and others,

397   2021). We note that a stitching approach can also be taken with our X-ray method using serially

398   cut ice blocks, which, when combined with recent advancements in 3D image correlation, could

399   eliminate many uncertainties and address large grain sizes. Effectively, the sample volumes we

400   imaged here balance the pros and cons of relatively large samples for lab-based DCT and

401   provide the option to collect lower- versus higher-resolution data to fit scientific questions.

402

403   3.2 Contrasts between 3D and 2D grain size distributions

404   Ice rheology has both crystal orientation and grain size dependencies (Cuffy and others,

405   2000; Durand and others, 2006). How these characteristics vary across ice layers largely reflects

406   the deformation mechanisms driving the viscous flow of ice sheets under their own weight

407   (Ranganathan and others, 2021). Crystal orientation fabrics and grain sizes, however, are

408   commonly decoupled (Svensson, Baadsager, and others, 2003; Faria and others, 2014). In thin

409   sections, the cross-sectional areas and shapes of grains change depending on burial depth,

410   temperature, amount of shear, or impurity concentrations. Observed trends between grain

411   area (2D) distributions and depth have led to informative grain growth models, although it has

412   been acknowledged that grain volume (3D) data would better suit these models (Svensson,

413   Schmidt, and others, 2003).

414   **Figures 4 and 5** demonstrate how volumetric data from 3D grain maps can be used to

415   assess the representativeness of 2D grain size distributions, which are the standard calculations

416   typically made using vertically, and sometimes horizontally, cut surfaces of ice cores (Faria and

417   others, 2014). While there are many ways glaciologists go about these calculations, we chose to

418   compare 3D and 2D grain size distributions by calculating equivalent sphere and circle

419   diameters of grains from their volumes and cross-sectional areas, respectively. We also extract

420   the major- and minor-axis lengths of grains based on ellipsoid (3D) and ellipse (2D) fitting. We

421   show in **Figures 4 and 5** how vertical and horizontal cuts can impose bias on grain size

422   measurements and related calculations (also see **Figures S2 and S3**). This is a well-known

423   problem that continues to motivate refinement of statistical correction methods, as a single 2D

424   measurement cannot capture the full grain shape and must be based on additional assumptions

425   (e.g., Morgan and Jerram, 2006; Mangler and others, 2022; Bretagne and others, 2023). To

426   demonstrate this dimensional bias statistically, we digitally cut the sample volume into vertical

427   and horizontal serial sections at intervals equal to the 60 µm voxel size of the DCT grain map.

428   This enabled us to measure the mean circle (2D) diameter of each grain against its spherical

429   (3D) diameter, while noting the full range of circle diameters encountered (**Figs. 4 and 5**). We

430   find that, on average, grain sizes would be severely underestimated in vertical cuts of our

431   samples, whereas grain sizes in horizontal cuts would be comparatively more representative

432   but with many overestimations (i.e. with respect to equivalent sphere and circle diameters).

433   Using the major-axis, for example, consistently leads to underestimations of grain sizes in these

434   samples (**Fig. 5 and S2**). These results indicate the influence of grain shapes and, in particular,

435   the effect of oblate or flattened grains in the horizontal plane, which becomes prevalent in

436   deep ice due to high compressive stress. Horizontal cuts may be significantly biased when

437   bimodal grain sizes are distributed unevenly or in layers, as in the NEEM sample (**Fig. 5**). As one

438   would expect, the probability of making a cut that yields a 2D grain size distribution matching

439   the 3D one will be greater for samples with more uniform grain shapes and sizes, but this is

440   improbable for samples containing high aspect ratio grains or varied sizes. Here we collectively

441   show how 3D grain maps provide insight into the relative contributions of grain shape versus

442   grain size, which may yield sample-specific correction factors for routine 2D grain size

443   calculations and help refine models of grain development and their utility (cf. Thorsteinsson

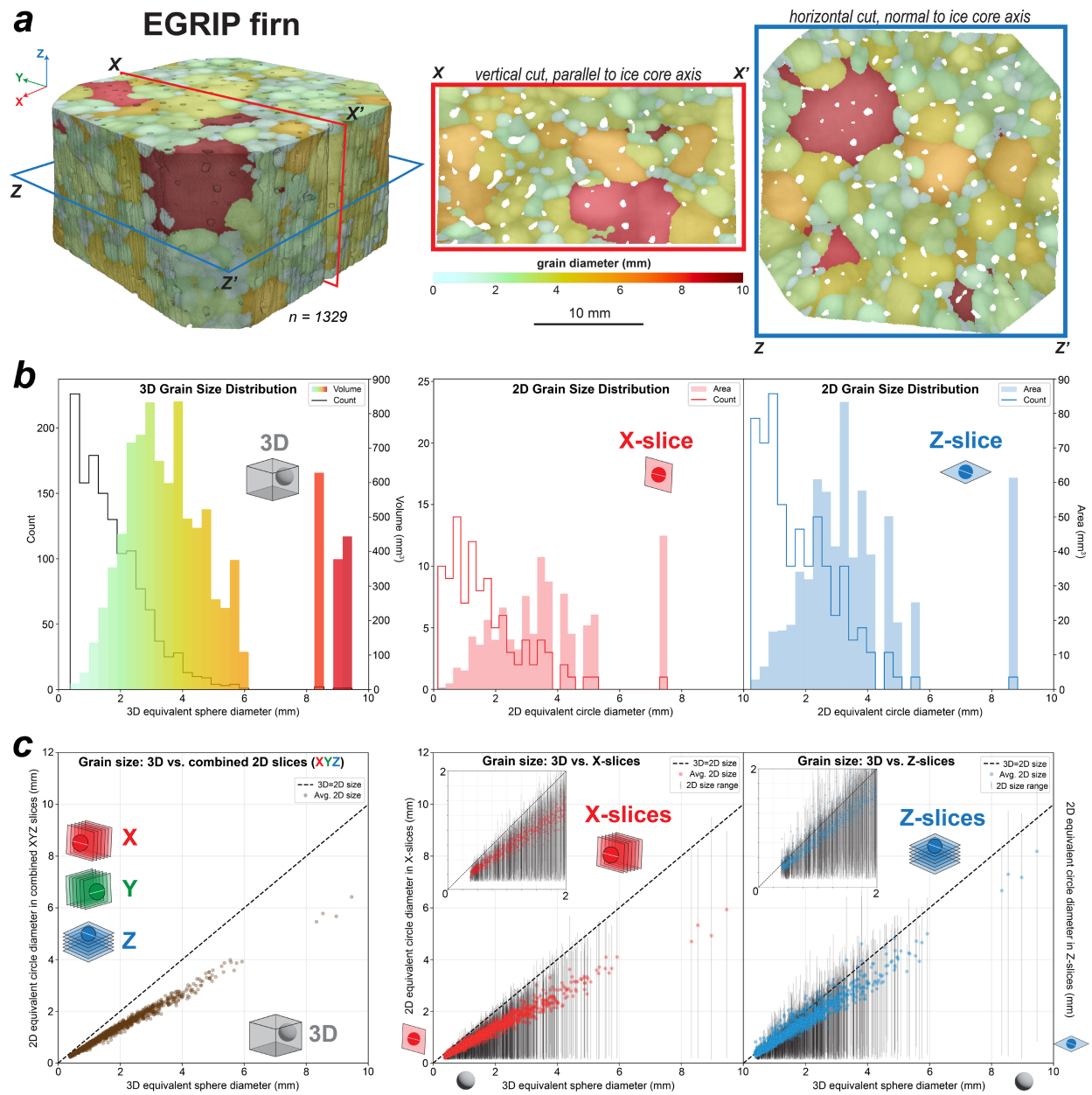444   and others, 1997; Svensson, Schmidt, and others, 2003; Rollet and others, 2017).

445

Figure 4. Comparing grain size information between 3D grain maps and virtual 2D slices of the EGRIP firn sample. **(a)** The 3D grain map, colored by grain diameter, was sliced orthogonally. **(b)** Grain size distributions based on 3D data are compared to those calculated in single, orthogonal X and Z section planes through the sample, which simulate vertical (X) and horizontal (Z) cuts typically made of ice cores. **(c)** Multiple XYZ slices in these plots represent 60 μm intervals (i.e., the reconstructed voxel size of DCT data). Grain sizes calculated from 3D volumetric data are plotted against grain sizes calculated from combined XYZ orthogonal slices, hence the 1:1 line, as well as the average 2D size of each grain found across XYZ slices combined. Each grain's average size based on either all X-slices or all Z-slices is also

455   compared to its volume-calculated size, with the full 2D size range for each grain plotted as vertical bars.

456   Note that all plot diameters represent equivalent sphere (3D) or circle (2D) diameters.
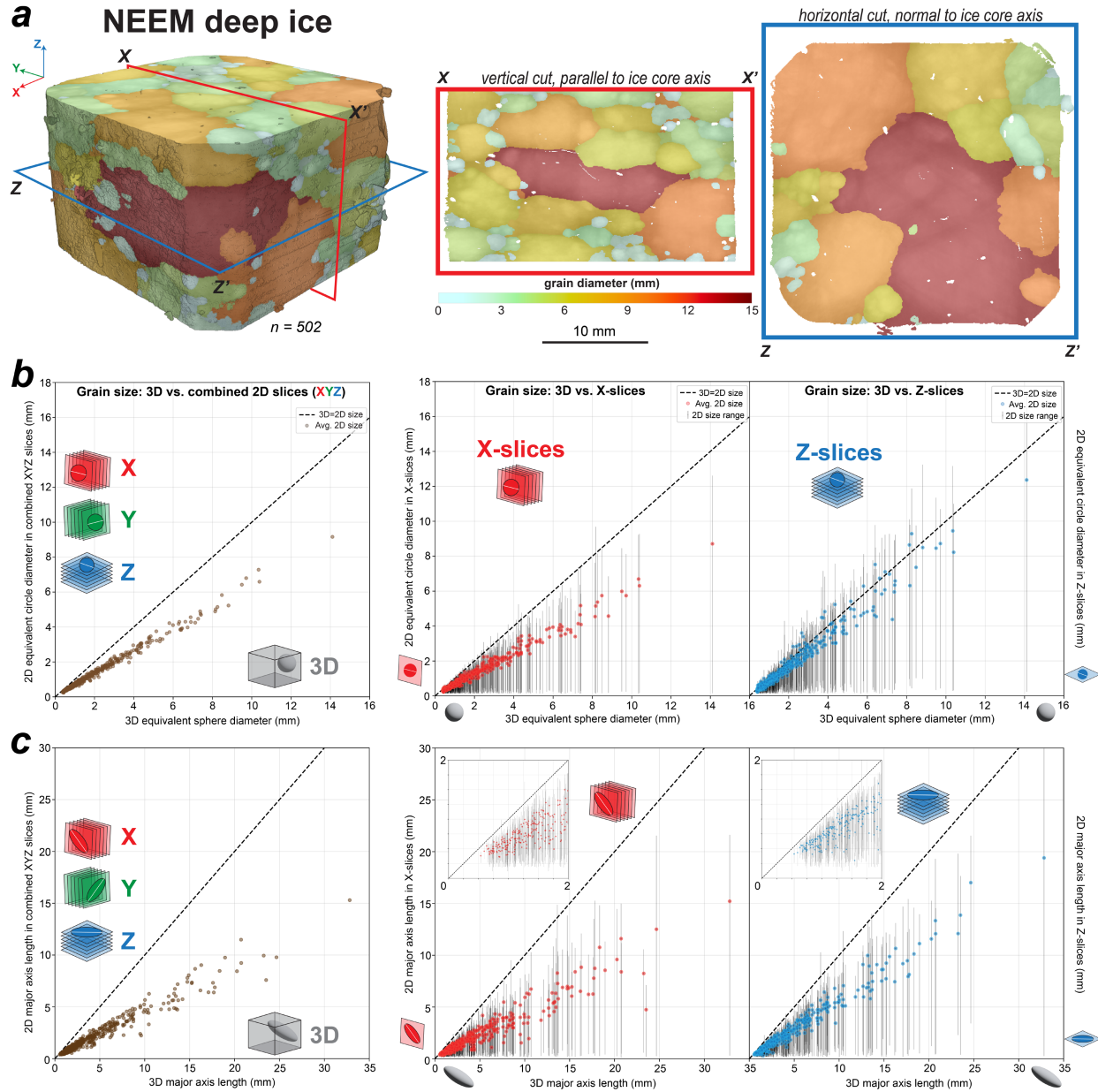
457

458

Figure 5. Comparing grain size information between 3D grain maps and virtual 2D slices of the NEEM

deep ice sample. **(a)** The 3D grain map, colored by grain diameter, was sliced orthogonally. X and Z slices

simulate the typical vertical (X) and horizontal (Z) cuts made of ice cores. **(b-c)** Multiple XYZ slices in

these plots represent 60 μm intervals (i.e., the reconstructed voxel size of DCT data). Grain sizes

calculated from 3D volumetric data are plotted against grain sizes calculated from combined XYZ

464 orthogonal slices, hence the 1:1 line, as well as the average 2D size of each grain found across XYZ slices

465 combined. Each grain's average size based on either all X-slices or all Z-slices is also compared to its

466 volume-calculated size, with the full 2D size range for each grain plotted as vertical bars. Note that **(b)**

467 plots diameters represent equivalent sphere (3D) or circle (2D) diameters, whereas **(c)** plots the major-

468 axis lengths of grains based on ellipsoid (3D) and ellipse (2D) fitting.

469

470 ## 3.3 Crystallographic fabrics characterized by grain size and *c*- and *a*-axes

471 Glacial ice behaves like a plastically deforming monomineralic rock. Its creeping flow

472 causes crystallographic fabrics and structures to develop, like those in high-grade metamorphic

473 rocks of Earth's crust and mantle. The fabrics are manifestations of a mechanical anisotropy

474 that develops slowly through intracrystalline glide on the basal plane of ice, normal to the *c*-axis

475 of its hexagonal crystal structure (Duval and others, 1983). While there are several dislocation

476 slip systems in ice, the basal slip dominates deformation and explains why the *c*-axis

477 preferentially tends toward the direction of compressional stress (Weikusat and others, 2017).

478 As a result, polycrystalline ice becomes more difficult to compress as the basal planes of more

479 and more grains become perpendicular to the compressive direction (Durand and others,

480 2006). Therefore, it is necessary to track the strength and evolution of *c*-axis fabrics to

481 determine the induced mechanical anisotropy, which has bearing on calculations of the large-

482 scale flow rates of ice sheets (e.g., Azuma, 1994; Montagnat, Castelnau, and others, 2014; Faria

483 and others, 2014; Fan and others, 2021). However, because slip is not necessarily isotropic in

484 the basal plane (Kamb, 1961), directions of the three *a*-axes are, in principle, also needed to

485 fully characterize deformation and might be a useful source of information to discern between

486 models of fabric evolution. Yet, crystal *a*-axes are largely uncharacterized for polar ice cores

487 because standard optical techniques, being the universal Rigsby stage and automatic fabric

488 analyzer, simply cannot be used to measure them (Rigsby, 1951; Langway, 1958; Russel-Head

489 and Wilson, 2001; Wilen and others, 2003). Methods used to simultaneously measure *c*- and *a*-

490 axes in the past, like etching and spot-based Laue X-ray diffraction, are time-intensive and

491 impractical (e.g., Matsuda, 1979; Miyamoto and others, 2011; Weikusat, Miyamoto, and others,

492 2011). Although modern cryo-EBSD can measure *c*- and *a*-axes and offers advantages in speed,

493 resolution, and angular precision, it is destructive and does not currently offer volumetric

494　information necessary to fully characterize CPOs (Weikusat, de Winter, and others, 2011; Prior

495　and others, 2015).

496　　　　Our coupled measurements of grain volume and full crystallographic orientation enable

497　us to interrogate fabrics in ways not previously possible. For example, in **Figures 6 and 7**, we

498　use volume-weighted pole figures to characterize fabrics at different grain size fractions and

499　compare them to traditional point-scatter and number-weighted pole figures that include all

500　grains. The comparison shows that weighting by volume versus number of grains does not

501　result in a significant difference in the distribution of crystal axis directions for our specific

502　samples, but the magnitudes of the distributions differ and may be relevant to different

503　questions concerning anisotropy. Such comparisons could be notably different for other ice

504　samples, like those with more diverse grain size distributions.

505　　　　Notably, we observe *c*-axis distributions commonly documented in ice cores, including

506　multimaxima, a broad or tight maximum around vertical, and a vertical girdle distribution,

507　which can be superimposed when plotting all grain sizes together. In other words, we identify

508　that different grain-size populations can contribute differently to the overall fabric developed in

509　each of our samples (**Figs. 6 and 7**; also see **Figure S4**). Therefore, 3D grain-population fabrics

510　could shed light on deformation or recrystallization mechanisms as they relate to grain size or

511　shape, for example, and may potentially be used to differentiate overprinted kinematics and

512　deformation drivers (Weikusat and others, 2017; Qi and others, 2019; Fan and others, 2020;

513　Stoll and others, 2024). Additionally, while several studies have used high grain number

514　statistics to conclude that fabric strength can develop independently of grain size with depth,

515　those relationships were assessed based on measured changes in the mean crystal area across

516　thin sections (e.g., Svensson, Schmidt, and others, 2003; Svensson, Baadsager, and others,

517　2003). Pulling apart fabrics using volume-based grain populations, in hindsight, may even

518　permit improved interpretations of optical thin-section images that cover centimeters to

519　meters worth of ice cores.

520　　　　Segregating *c*-axis fabrics can ultimately help characterize *a*-axis fabrics, a challenge

521　inherent to the presence of three indistinguishable *a*-axes in the basal plane. Distributions of *a*-

522　axes appear considerably weaker by comparison, therefore we plot *a*-axes on a separate scale

523   unbound by the intensity of *c*-axis CPOs in **Figures 6 and 7**. For most grain size fractions in our

524   samples, the *a*-axes define a broad girdle that hosts multimaxima on a plane roughly normal to

525   the ice-core axis; whereas, *a*-axes of the largest grain sizes can deviate away from this plane

526   considerably. The mere presence of *a*-axis CPOs in our data is significant and corroborates

527   those observed in experiments and mountain glaciers, collectively indicating that slip is

528   anisotropic in the basal plane wherein *a*-axes lie (Kamb, 1961; Montagnat and others, 2015; Qi

529   and others, 2019; Journaux and others, 2019; Monz and others, 2021). This suggests that *a*-axes

530   may contribute more to fabric development and therefore mechanical properties of ice sheets

531   than is currently accounted for. We note, however, that because ice cores rotate when they are

532   drilled and brought to the surface, the unconstrained nature of pole figures may make it

533   challenging to interpret *a*-axis CPOs geographically, likely requiring statistically robust datasets

534   to fully evaluate their importance. Despite this challenge, access to *a*-axis information can

535   potentially provide a different avenue for validating homogenization schemes of

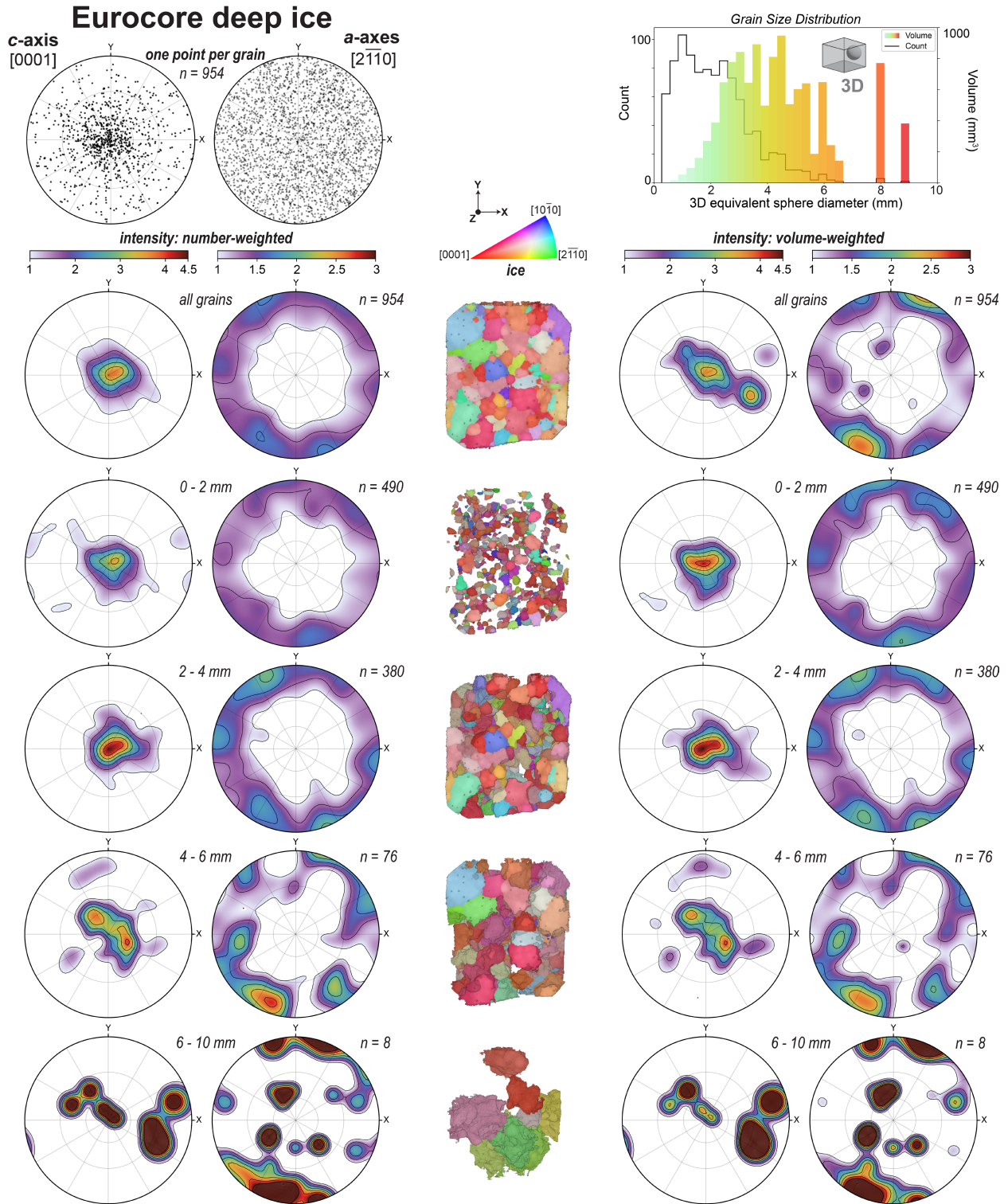536   micromechanical models or to discern between these models, for example.

537

Figure 6. Comparing pole figure analysis for the Eurocore sample's grain orientations based upon count, volume, and grain size fraction. Pole figures provide views down the sample Z-axis, parallel to the ice-core axis. Analytical details are provided in the **Methods**. Note that glaciological studies employing EBSD

542   of ice may instead represent the *a*-axes as $[11\bar{2}0]$ (-a_3), which is symmetrically equivalent to $[2\bar{1}\bar{1}0]$ (+a_1)
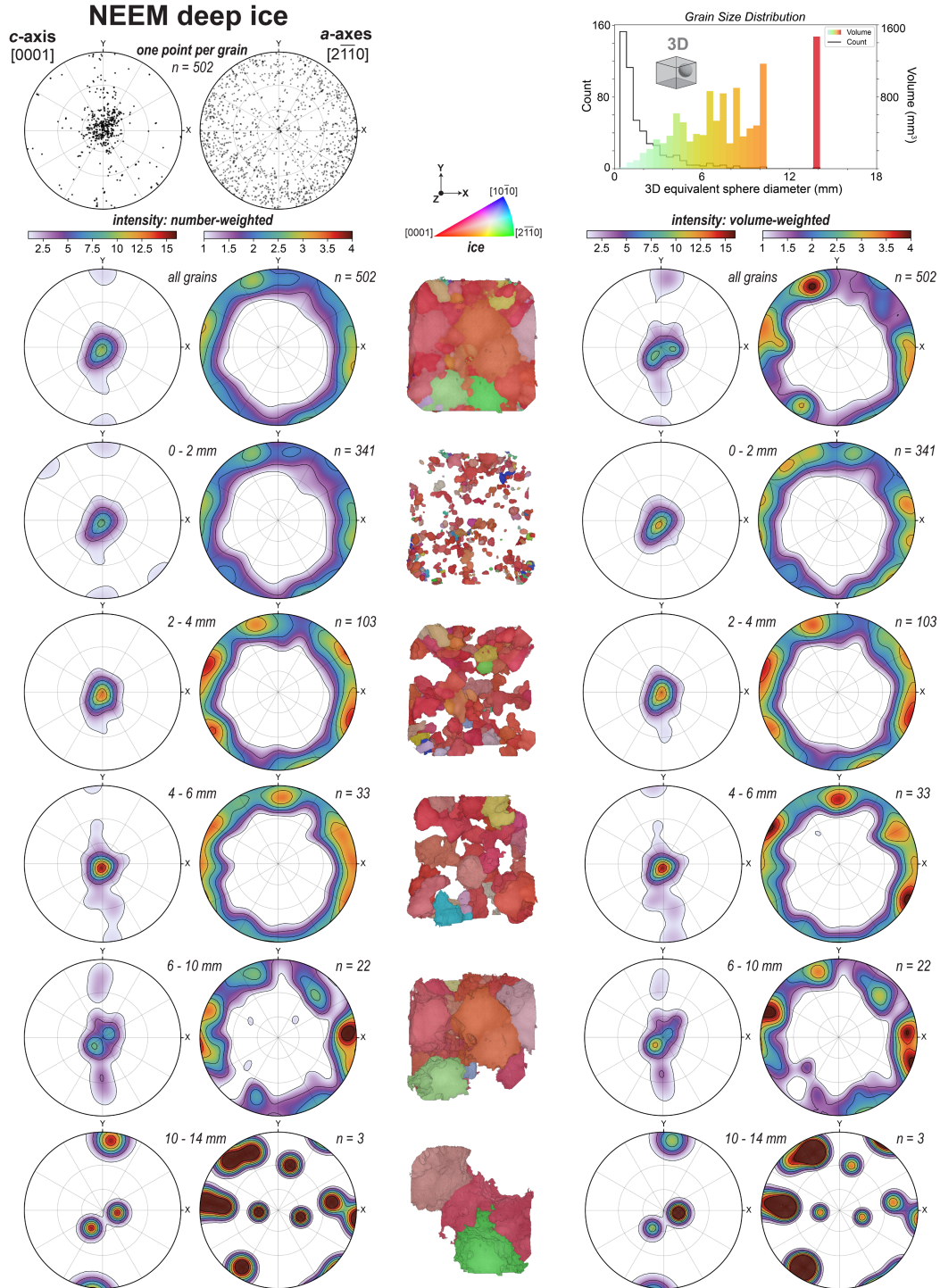
543   (e.g., see Qi and others, 2019).

544

Figure 7. Comparing pole figure analysis for the NEEM sample's grain orientations based upon count,

volume, and grain size fraction. Pole figures provide views down the sample Z-axis, parallel to the ice-

core axis.

548

3.4 Misorientations across grains

549

550 Many microscopic mechanisms operate during ice deformation and to different extents

551 over the depth of ice sheets, ultimately affecting the ice's macroscopic flow behavior

552 (Thorsteinsson and others, 1997; De La Chapelle and others, 1998; Montagnat and others,

553 2015; Ranganathan and others, 2021). Recrystallization mechanisms activate to reduce the

554 strain energy that accumulates as neighboring grains interact and develop internal stress and

555 strain fields that can be highly heterogeneous near grain boundaries (Duval and others, 1983;

556 Montagnat and others, 2015). These processes can lead to grain boundary migration, grain

557 growth, or nucleation and introduce crystal lattice dislocations that manifest as substructures

558 and subgrain boundaries (Montagnat and others, 2015; Rollet and others, 2017).

559 Measuring crystallographic misorientations across grains is commonly used to

560 understand areas of high dislocation density and recrystallization mechanisms. In this context,

561 cryo-EBSD has proven highly useful for mapping low-angle misorientations at resolutions of 10

562 μm or higher, although some studies have employed lower (e.g., 50 μm) resolutions to

563 characterize subgrains (e.g., Montagnat and others, 2015, also see Weikusat, Miyamoto, and

564 others, 2011). Optical-based techniques, like AFAs, similarly provide a high (6 μm) spatial

565 resolution but a lower angular resolution (3°) compared to EBSD (0.1-1°) (Prior and others,

566 1999; Winkelmann and others, 2020). However, cryo-EBSD and AFAs share the same

567 disadvantages in that they can only uncover information from cut surfaces, which generates

568 uncertainties in the representation of grain shapes and sizes. In contrast, lab-based DCT can

569 offer a spatial resolution down to about 30 μm for our specific sample sizes and a high (0.1°)

570 angular resolution (Sun and others, 2022). While the 2D-based techniques can cover large

571 sample areas (up to 7 x 3 cm for EBSD and 10 x 10 cm for AFA; Prior and others, 2015, Faria and

572 others, 2014), DCT provides the advantage of working with bulk samples that yield volumetric

573 information and maintain 3D contexts crucial to interpretations. Therefore, a correlative 3D-2D

574   microscopy method could generate complementary data sets that offer powerful multiscale,

575   multidimensional information.

576   Our large sample volume, experimental setup, and DCT measurements permitted

577   realistic grain map reconstructions down to 60 μm voxel sizes, comparable to EBSD resolutions

578   applied previously (e.g., Montagnat and others, 2015). At this resolution, we were able to

579   resolve what appear to be subgrains, whose boundaries strongly correspond to those seen in

580   grain completeness maps (**Figure 3**), corroborating the evidence of intracrystalline deformation

581   in X-ray diffraction patterns (**Figure S1**). Notably, the density and degree of misorientations

582   appear dependent on the size and average orientation of a grain, but these relationships vary

583   with ice depth and degree of deformation. Specifically, smaller grains in the EGRIP firn sample

584   tend to exhibit higher misorientations across distinct subgrain boundaries, yet a relation to the

585   average grain orientation appears weak. Conversely, in the Eurocore and NEEM samples, larger

586   grains tend to show a much higher density of internal misorientations than the very smallest

587   grains, but the degree of misorientation varies between larger grains, indicating a possible

588   dependency on the average grain orientation with respect to far-field or even local stresses

589   (also see Section 3.5). Distinct subgrains are observed least in the very largest grains of these

590   deep ice samples. In the following section, we integrate these observations with those of

591   bubble shapes and discuss how 3D misorientation data could help constrain grain-scale

592   deformation histories.

593

594   ## 3.5 Spatial relationships between ice grains and pore spaces

595   The decrease in ice sheet porosity with depth reflects the densification of accumulated

596   snow and its progressive burial and deformation. An interplay exists between air-bubble and

597   grain-scale processes that must be understood when it comes to (1) measuring atmospheric

598   gases trapped in ice cores and (2) constraining controls on ice deformation. Knowing precisely

599   where and how air bubbles are occluded in the firn column is crucial for determining the age

600   difference between bubbles and the encapsulating ice (Burr and others, 2018; Westhoff and

601   others, 2024). Similarly, knowing where atmospheric gases become occluded in clathrates

602   under immense compression at depth, as well as how ice-core relaxation affects the

603   retransformation of clathrates to air bubbles, is crucial for understanding gas behavior (e.g.,

604   Pauer and others, 1996; Kipfstuhl and others, 2001). Further, knowing how grain-growth

605   mechanisms (that help to seal bubbles) are affected kinetically by the bubbles themselves is

606   important for understanding grain-scale deformation near the firn-ice transition (Roessiger and

607   others, 2014; Fegyveresi and others, 2019; Fan and others, 2023). Anisotropic bubble shapes in

608   deep ice may also record the stress distribution on individual grains and improve our

609   understanding of local and far-field stresses needed to model ice flow.

610   In **Figures 8-11**, we demonstrate how correlating bubbles (generally pores) with the 3D

611   grain structure allows an integration of qualitative and quantitative information that is difficult

612   to access from 2D sections of ice cores. By visualizing pores and grains as surface meshes

613   created from 3D maps, we can view bubbles from the perspective of their host-grain

614   orientations, which becomes a powerful guide for quantitative analysis.

615   Bubble position determined simply as intergranular versus intragranular is an important

616   parameter that provides insight on gas pathways, grain-growth behavior and ice-air boundary

617   mobility (e.g., grain-boundary migration and bubble pinning; Roessiger and others, 2014). In

618   **Figure 8,** we paired spatial classifications with bubble sizes and found expected differences

619   between the firn and deep ice samples. In the EGRIP firn sample, the size distribution of

620   bubbles that intersect grain boundaries is distinct from bubbles positioned wholly within grains.

621   Different types of bubbles are identifiable by their spherical, tube-like, or amoeboid shapes, the

622   latter two of which are visibly larger. Therefore, even without quantitative measures of the

623   complex bubble shapes, one can infer from the count and volume distribution data that more

624   non-spherical bubbles intersect grain boundaries (cf. Kipfstuhl and others, 2009). Differences

625   between inter- and intra-granular bubble size distributions in the Eurocore sample are more

626   subtle, consistent with grain growth increasing the numbers of intragranular bubbles in deeper

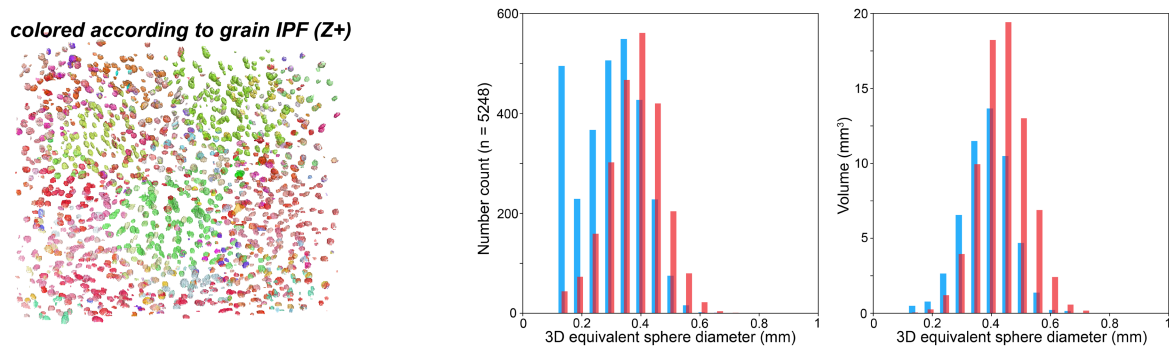627   ice (De La Chapelle and others, 1998).

628
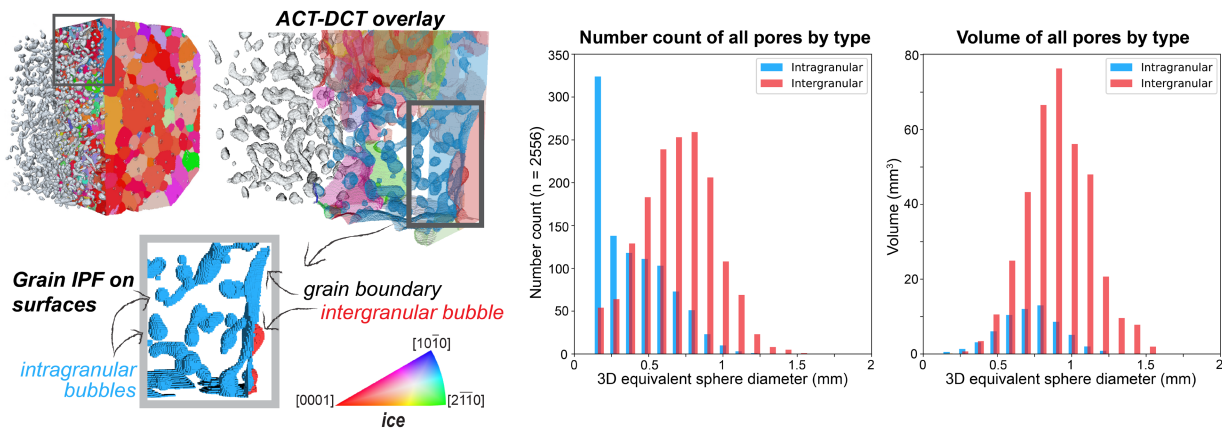
Figure 8. Size distributions of air bubbles categorized by their intergranular versus intragranular positions. Pore spaces in EGRIP firn and Eurocore deep ice samples represent primary air bubbles captured by ice during the densification process. The overlay of ACT and DCT surface meshes enable visualizations and correlations of bubbles and grain boundaries. Bubble surfaces are colored with respect to the IPF(Z+) color of their host grain(s) and therefore change color across the grain boundaries.

Bubble shapes in deep ice have been proposed as possible strain gauges, given bubbles deform ~1.7 times faster than the surrounding ice (Alley and Fitzpatrick, 1999; Fegyveresi and others, 2019). Previous data for elongated bubbles, as well as slightly nonspherical ones typical of deep ice cores, have led to the physical understanding that diffusion restores bubbles toward steady-state spherical shapes. Bubbles deform, however, if the diffusion rate is slower than that of deformation. Flattened or elongated bubbles are therefore thought to record strain rates and directions of deformation, which are expected to differ between grains and depend on both local and far-field stresses (Fegyveresi and others, 2019). A closer look at the Eurocore sample in **Figure 9** revealed bubble-shape anisotropies that are strongly grain-dependent. More

645   specifically, intragranular bubbles belonging to the same grain are visibly flattened and/or

646   elongated in roughly the same plane, but their sizes and aspect ratios vary (**Fig. 9**). Bubble-

647   shape orientations also tend to vary considerably near grain margins. Such observations are

648   consistent with those made previously in ice cores (e.g., Alley and Fitzpatrick, 1999; Fegyveresi

649   and others, 2019), however, past studies employed 2D techniques that imposed measurement

650   limitations, which did not allow bubble shapes to be used to their full potential.

651   For the 954 grains in the Eurocore sample, we analyzed 5248 bubbles, of which 2647 are

652   intragranular and do not intersect the sample margins (see **Methods**). Of these intragranular

653   bubbles, approximately 65% are oblate (disk-shaped), 15% are prolate (rod-shaped), and 20%

654   are roughly spherical in shape (ellipsoid factor of -0.05 ≤ x ≤ 0.05) (**Figs. 9 and 10**). There are no

655   clear correlations between bubble shape, volume, and host-grain volume in this sample (**Fig.**

656   **10**; **Fig. S5**). There is a strong correlation, however, between the directions of bubble-

657   flattening/elongation and the *c*-axis and basal plane of the host grain (**Fig. 9**). An analysis of all

658   2647 intragranular bubbles indicates they have a strong preference to flatten and elongate in

659   the grain basal plane, the dominant slip plane in ice during deformation. Based on bubble

660   major-axis directions, we determined that 76% of them are elongated within 20° of the basal

661   plane (**Fig. 9**), while 57% are within 10°. The minor-axis directions indicate that 57% of bubbles

662   have a flattening, or shortening, direction within 20° of the *c*-axis. How the host grain is

663   oriented relative to the compressive direction (Z) does not appear to control the angle between

664   the directions of bubble-flattening/elongation and the *c*-axis or basal plane, suggesting a strong

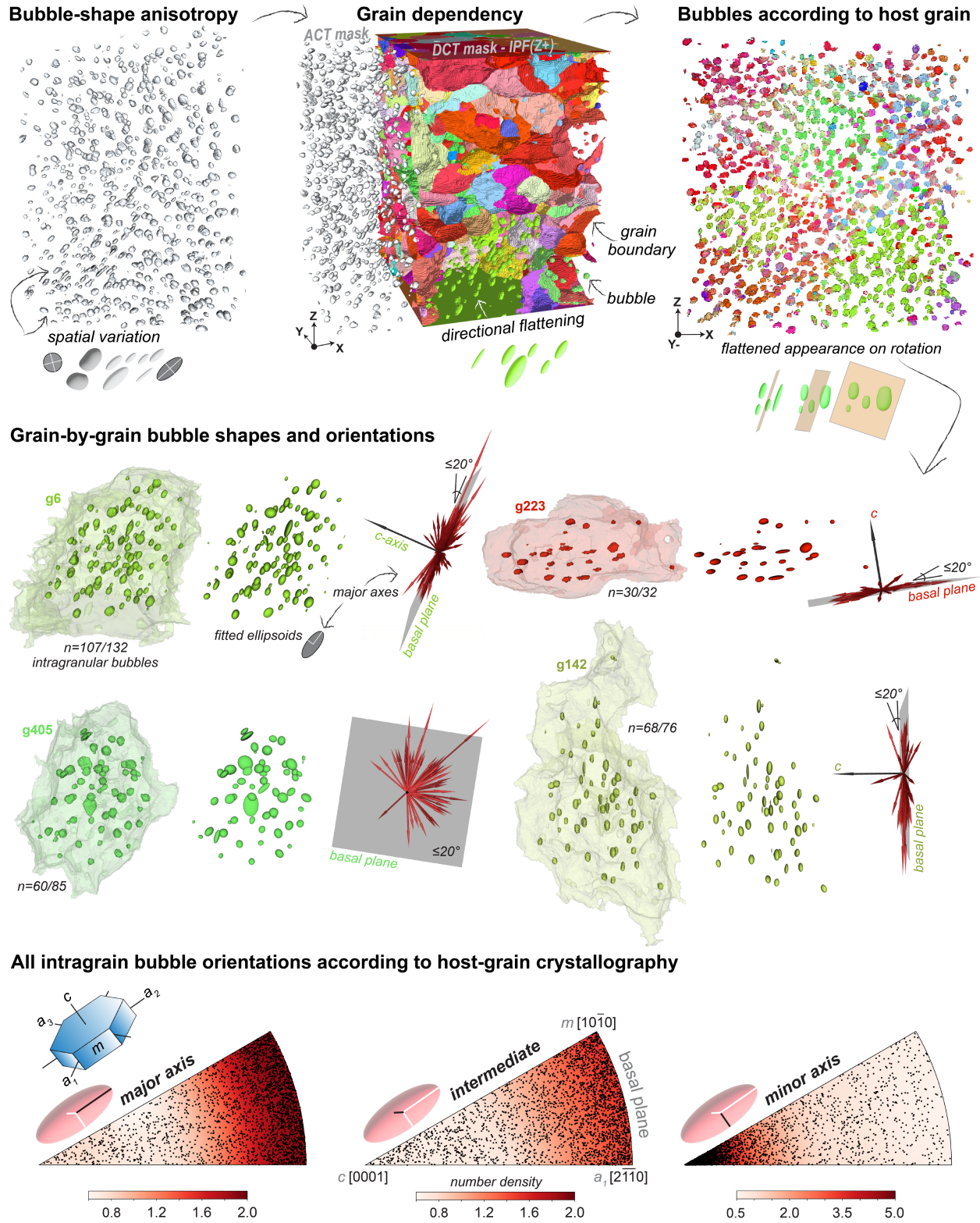665   crystallographic control (see **Figure S6**).

666

Figure 9. Bubble-grain relationships identified through correlative, multimodal imaging. Bubble-shape

anisotropies in the Eurocore sample were first observed using an ACT-derived surface mesh (gray). By

670 overlaying the ACT bubble-surface mesh with a grain-surface mesh generated from the DCT volume (IPF

671 color), the visualization of ACT bubbles colored by the IPF orientation of their host grain(s) led to the

672 observation that bubble anisotropy is grain-dependent. Rotation of the sample revealed most bubbles

673 inside the same grain exhibit flattening and/or elongation in roughly the same plane, although variability

674 occurs near grain boundaries. The three largest grains (g6, g405, g142) and another grain (g223) with its

675 *c*-axis near-vertical (Z) are shown with intragranular bubbles and their fitted ellipsoids (see **Methods**).

676 Major-axes of the ellipsoids are plotted as red vectors scaled by the ellipsoid aspect ratio, and only for

677 bubbles whose major-axis lies within 20° of the grain basal plane (the number fraction of these bubbles

678 is given as *n* for each grain). The dominant oblateness of bubbles with preferential flattening and/or

679 elongation in the grain basal plane is expressed collectively by IPFs of the fitted-ellipsoid axes. The IPFs

680 represent all intragranular bubbles plotted with respect to the crystallography of their host-grains,

681 which have been rotated into a single reference frame.

682

683   While some of our observations of bubble-grain relationships are comparable to those

684 of Fegyveresi and others (2019), their 2D optical technique offers measurements within one

685 section plane and typically only *projections* of elongations. In **Figure 10**, we demonstrate the

686 limited information we would gather from a single section plane through different grains in our

687 Eurocore sample. Only by searching and selecting slices through 3D data could we find bubbles

688 with the highest *projected* "elongation" that could then be verified against a *projection* of the

689 host-grain *c*-axis (determined from pole figures). Accurate measures and the true spatial

690 variability of bubble shapes across the bulk sample would never be captured without 3D

691 information in this case. Nonetheless, we find it interesting that Fegyveresi and others (2019)

692 found correlations between bubble shape, size, and grain size in their Antarctica sample,

693 whereas we do not see clear trends. Although we can identify that grain size and the density of

694 internal grain misorientations are roughly correlated (see section 3.4, **Fig. 10**), we do not see a

695 clear relationship between these characteristics and the magnitude of bubble-

696 flattening/elongation, for example. One possibility is that grain-scale interactions generate

697 differences between local and far-field stresses, resulting in different deformation rates for

698 individual grains and variance in observable patterns (Fegyveresi and others, 2019). We suggest

699 another possibility is that the Eurocore sample's bubbles have undergone enough diffusional

700 restoration to erase any such correlations, if they ever existed. After all, the current bubble

701 configurations can be assumed to represent both the cumulative deformation and the balance

702 between diffusion and deformation over the entire history of the ice (Fegyveresi and others,

703 2019).

704

705
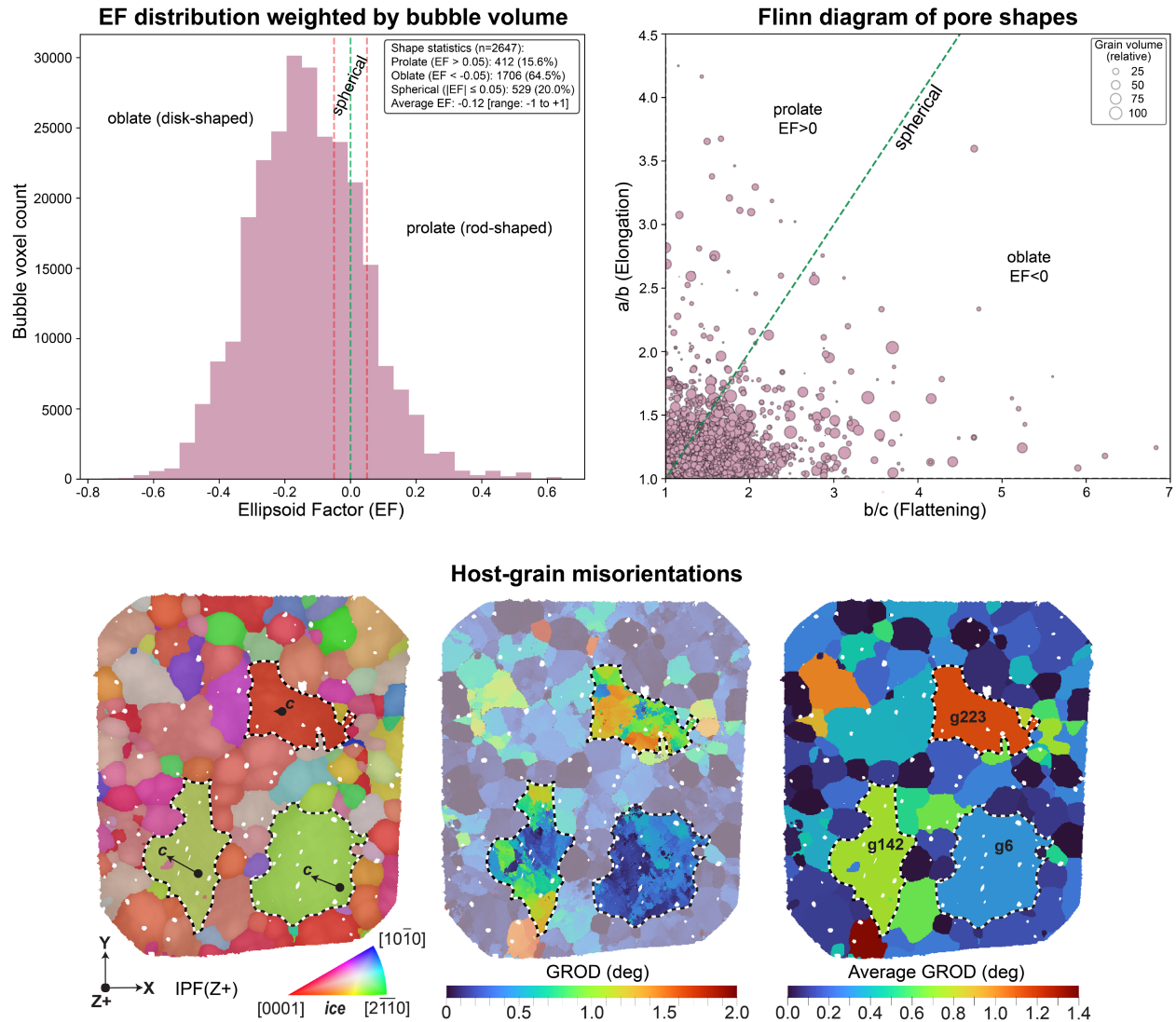
Figure 10. Examples of possible relationships and non-relationships among intragranular bubbles and

their host-grains in the Eurocore sample. The ellipsoid factor (EF) was used to classify bubbles as prolate,

oblate, or spherical based on their fitted ellipsoids. As depicted in the EF distribution plot, the

boundaries for "spherical" bubbles were chosen at -0.05 ≤ EF ≤ 0.05. The Flinn diagram reflects these

shape classifications but adds information about host-grain volume, which has been normalized. A single

711   slice through the 3D grain map intersects three of the grains isolated in **Figure 9**, which are among the

712   eight largest grains. Notably, these grains show a relatively high density of intragranular, low-angle

713   misorientation boundaries but different average-GROD values.

714

715   On the other hand, at depths greater than the Eurocore sample, immense compression

716   causes gases to transform into clathrates and leads to the eventual loss of all original bubbles in

717   ice. However, following the recovery of bubble-free ice cores, the stress release can cause

718   fractures to form and bubbles to redevelop from clathrates (e.g., Pauer and others, 1996;

719   Kipfstuhl and others, 2001). These secondary processes have received considerable attention

720   because they may lead to gas escape and affect gas concentration measurements that are

721   notably destructive for ice cores.

722   The pore spaces in the NEEM sample are bubbles and cracks that have formed from

723   decomposed clathrates and relaxation since the core was drilled in 2010, although many pores

724   have a flattened, yet graupel-like appearance characteristic of primary clathrates (Pauer and

725   others, 1996; Kipfstuhl and others, 2001). These features are interesting because most pores

726   and apparent fracture planes have a strong preference to align with the basal plane of the host

727   grain (**Fig. 11**). We determined this by analyzing all 2424 intragranular pores (out of 3276 total

728   pores) for the 502 grains identified in the sample. The NEEM pore results (**Fig. 11**) are

729   remarkably similar to those of the Eurocore sample (**Fig. 9**), suggesting that the grain

730   crystallography may also exert a strong crystallographic control on relaxation processes and the

731   evolution or retransformation of clathrates. The visualization and statistical analysis of 3D sizes,

732   shapes, and spatial distributions of these features could be paired with Raman spectroscopy

733   (Pauer and others, 1996), for example, to contextualize and ensure accurate measurements of

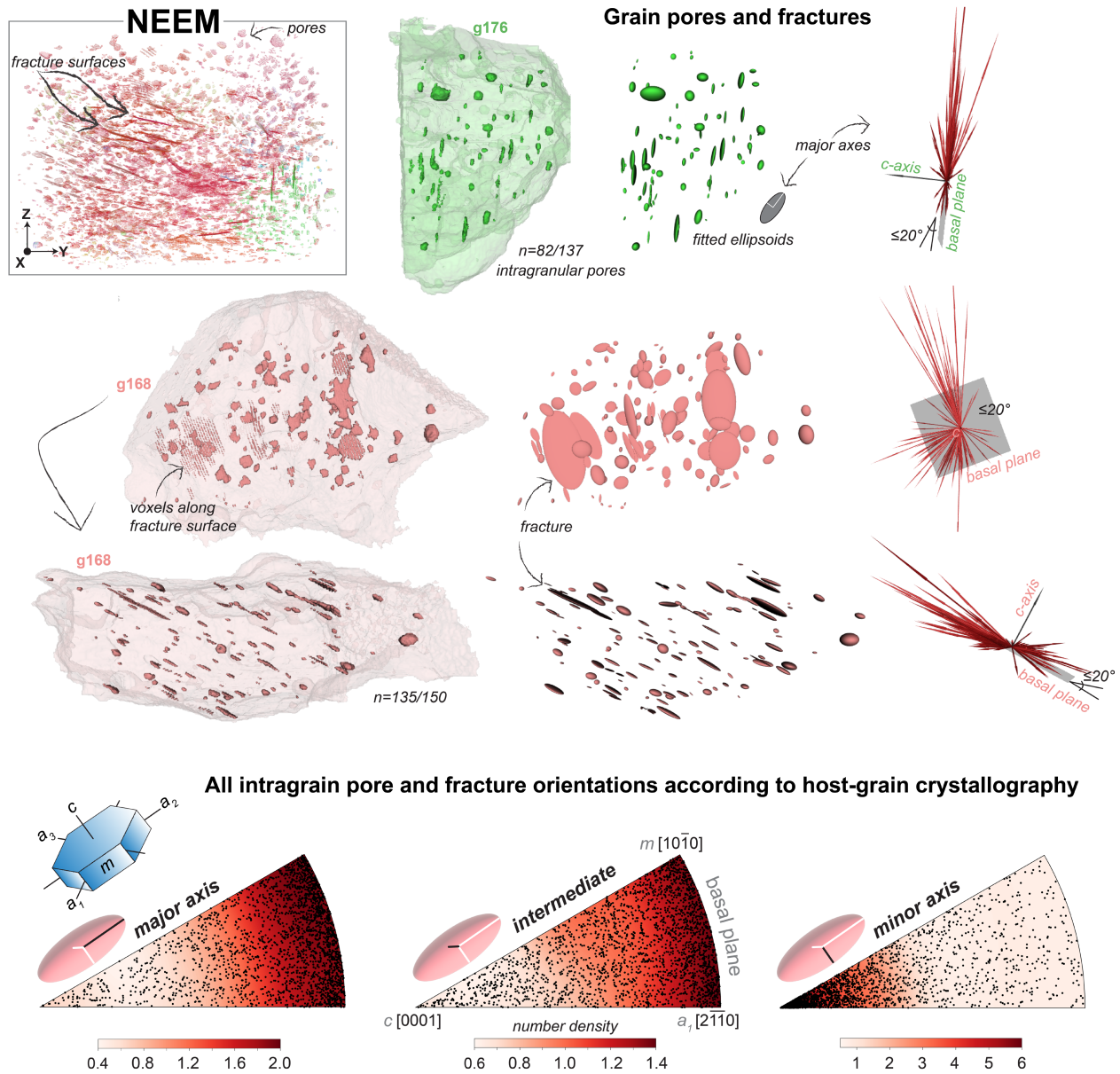734   the ancient atmospheric gases in ice cores.

735

Figure 11. Pore-grain relationships in the NEEM sample. The visualization of pore spaces and apparent microfractures throughout the sample (top left) were performed in the same way as described for the Eurocore sample in **Figure 9**. Two of the largest grains with the *c*-axis near-vertical (g168) or near-horizontal (g176) with respect to the ice-core axis are shown with intragranular pores and their fitted ellipsoids (see **Methods**). Grain 168 is shown in two different views; one view looks down the *c*-axis and the other looks normal to it. The features we refer to as microfractures are very thin and require careful segmentation of our data to preserve the fracture surfaces, which, at our data resolution, appear as adjacent lines of voxels. Our connected component analysis allowed the merging of these neighboring

745 voxels to fit an ellipsoid to each fracture. The vector plots and IPFs here are the same as described for

746 **Figure 9**.

747

4 CONCLUSIONS

749 Our pilot study demonstrates that ice core microstructures, fabrics, and air bubbles can

750 be imaged in 3D using multimodal X-ray imaging in a lab setting. We show that samples as large

751 as 3 x 3 x 3 cm^3 are achievable and balance the advantages and disadvantages of imaging what

752 are considered large volumes for the multimodal X-ray technique. These sample sizes allowed

753 us to achieve adequate resolutions and volume-based statistics under reasonable acquisition

754 times, and they provide the opportunity to vary the spatial resolution to investigate specific

755 scientific questions. Our novel method for measuring, mapping, and analyzing ice textures can

756 be combined with established ice-core analytical techniques to generate complementary 3D

757 and 2D datasets. Such datasets can maximize scientific insight through the benefits of 3D

758 sample curation, volumetric measurements, shape determinations with improved accuracy,

759 and the integration of complete ice-grain crystallographic orientations. Together, the analytical

760 method and our preliminary results demonstrate great potential for 3D textural data to

761 advance ice-core paleoclimate studies and the future development of more integrated models

762 of grain-scale ice deformation and large-scale ice flow.

763

5 OUTLOOK

765 Using 3D data to improve the performance of micromechanical and large-scale ice-flow

766 models will benefit from higher-resolution (<10 μm) multimodal scanning, which is needed to

767 resolve intracrystalline deformation features to a greater accuracy. Such high-resolution 3D

768 datasets would help constrain the complex behaviors of grains, bubbles, and potentially large

769 impurities as they interact during ice deformation, which is currently challenging to

770 parameterize in models. One caveat of going to higher resolutions is that the experiments will

771 require smaller, less representative sample volumes. This may entail design modifications to

772   the current cooling device, and perhaps the development of a correlative, multiscale approach

773   to data collection.

774   In general, our analytical method has the potential to advance the level of textural

775   characterizations of ice-core samples, and to implement those results into advanced ice-flow

776   models and paleoclimate reconstructions. Our preliminary results demonstrate the ability to

777   detect 3D variations in ice-core textures from different depths and climatic periods. Therefore,

778   examples of future studies that could apply our new method include (1) stratigraphic sampling

779   to investigate bubble closure, clathrate formation, grain-scale deformation, or the 3D evolution

780   of ice fabrics with depth, or (2) modeling ice-fabric evolution over the depth of the ice sheet

781   using *c*- and *a*-axis orientations of grains. Additionally, experimental studies could also employ

782   our method to understand, for example, (1) the effects of melting on ice textures using

783   controlled temperature changes and time-lapse experiments, or (2) the rates of microstructural

784   evolution and bubble/clathrate transformation under ambient pressure through interrupted

785   time-series experiments.

786

787   **AUTHOR CONTRIBUTIONS**

788   **O.A.B.**: Conceived the project, designed experiments, performed imaging, performed data

789   reconstruction, performed data visualization and analysis, created figure illustrations, wrote the

790   manuscript. **J.O.**: Performed simulations to guide experimental design, supported imaging and

791   data reconstruction, performed data post-processing, supervised the project. **R.R.P.P.R.P.**:

792   Wrote code for data analysis and visualization, performed data analysis; **H.W.Å.**: Wrote code

793   for data analysis and visualization, performed data analysis. **J.E.**: Designed experiments, built

794   and tested the cooling device. **A.S.**: Selected and prepared samples, provided scientific insight

795   and discussion. **N.M.R.**: Provided scientific insight and discussion. **T.B.**: Provided scientific

796   insight and discussion. **F.B.**: Provided data reconstruction and software support. **S.H.**:

797   Conceived and supervised the project, designed experiments. All authors contributed to the

798   final version of the manuscript.

799

800

801 **ACKNOWLEDGMENTS**

802 Discussions with members of the Physics of Ice, Climate and Earth group at the University of

803 Copenhagen are greatly appreciated. This work was supported by Innovation Fund Denmark

804 through a collaborative Industrial Postdoctoral Researcher grant (3130-00017B) awarded to

805 O.A.B., Xnovo Technology, and Lund University; J.O., S.H., and J.E. were also supported under

806 this grant. N.M.R. was supported by the Novo Nordisk Foundation Challenge grant no.

807 NNF23OC0081251. A.S. acknowledges funding from the European Union (ERC, *Green2Ice*,

808 101072180). Views and opinions expressed are those of the authors only and do not necessarily

809 reflect those of the European Union or the European Research Council Executive Agency.

810 Neither the European Union nor the granting authority can be held responsible for them.

811

812 **COMPETING INTERESTS**

813 The authors declare no competing interests.

814

815 **DATA AVAILABILITY**

816 Data reported in this paper are available on request given individual file sizes reach 10s of GB.

817

818 **REFERENCES**

819 **Alley RB** (1992) Flow-law hypotheses for ice-sheet modeling. *Journal of Glaciology* **38**(129),

820   245–256. doi:https://doi.org/10.3189/S0022143000003658.

821 **Alley RB and Fitzpatrick JJ** (1999) Conditions for bubble elongation in cold ice-sheet ice. *Journal*

822   *of Glaciology* **45**(149), 147–153.

823 **Ayachit U** (2015) *The paraview guide: a parallel visualization application.* Kitware, Inc., Clifton

824   Park, NY, United States. doi:10.5555/2789330.

825 **Azuma N** (1994) A flow law for anisotropic ice and its application to ice sheets. *Earth and*

826   *Planetary Science Letters* **128**(3–4), 601–614.

827 **Bachmann F, Bale H, Gueninchault N, Holzner C and Lauridsen EM** (2019) 3D grain

828   reconstruction from laboratory diffraction contrast tomography. *Journal of Applied*

829   *Crystallography* **52**(3), 643–651.

830   **Baker I** (2019) Microstructural characterization of snow, firn and ice. *Philosophical Transactions*

831   *of the Royal Society A: Mathematical, Physical and Engineering Sciences* **377**(2146).

832   **Bendel V and others** (2013) High-resolution variations in size, number and arrangement of air

833   bubbles in the EPICA DML (Antarctica) ice core. *Journal of Glaciology* **59**(217).

834   doi:10.3189/2013JoG12J245.

835   **Binder T, Garbe CS, Wagenbach D, Freitag J and Kipfstuhl S** (2013) Extraction and

836   parametrization of grain boundary networks in glacier ice, using a dedicated method of

837   automatic image analysis. *Journal of Microscopy* **250**(2), 130–141.

838   **Bretagne E, Wadsworth FB, Vasseur J and Dobson KJ** (2023) A Scaling for the Permeability of

839   Loose Magma Mush Validated Using X-Ray Computed Tomography of Packed

840   Confectionary in 3D and Estimation Methods From 2D Crystal Shapes. *Journal of*

841   *Geophysical Research: Solid Earth* **128**(10), e2023JB026795.

842   **Burr A, Ballot C, Lhuissier P, Martinerie P, Martin CL and Philip A** (2018) Pore morphology of

843   polar firn around closure revealed by X-ray tomography. *Cryosphere* **12**(7), 2481–2500.

844   doi:10.5194/TC-12-2481-2018.

845   **Cuffey KM, Thorsteinsson T and Waddington ED** (2000) A renewed argument for crystal size

846   control of ice sheet strain rates. *Journal of Geophysical Research: Solid Earth* **105**(B12),

847   27889–27894. doi:10.1029/2000JB900270.

848   **Disbrow-Monz ME, Hudleston PJ and Prior DJ** (2024) Multimaxima crystallographic fabrics

849   (CPO) in warm, coarse-grained ice: New insights. *Journal of Structural Geology* **182**,

850   105107.

851   **Durand G, Gagliardini O, Thorsteinsson T, Svensson A, Kipfstuhl S and Dahl-Jensen D** (2006)

852   Ice microstructure and fabric: an up-to-date approach for measuring textures. *Journal of*

853   *Glaciology* **52**(179), 619–630. doi:10.3189/172756506781828377.

854   **Duval P, Ashby MF and Anderman I** (1983) Rate-controlling processes in the creep of

855   polycrystalline ice. *Journal of Physical Chemistry* **87**(21), 4066–4074.

856   **Fan S and others** (2023) Grain growth of natural and synthetic ice at 0 °c. *Cryosphere* **17**(8),

857   3443–3459.

858 **Fan S and others** (2021) Crystallographic Preferred Orientation (CPO) Development Governs

859   Strain Weakening in Ice: Insights From High-Temperature Deformation Experiments.

860   *Journal of Geophysical Research: Solid Earth* **126**(12), e2021JB023173.

861 **Fan S and others** (2020) Temperature and strain controls on ice deformation mechanisms:

862   Insights from the microstructures of samples deformed to progressively higher strains at

863   −10, −20 and −30 ◦C. *Cryosphere* **14**(11), 3875–3905. doi:10.5194/TC-14-3875-2020.

864 **Fan S and Prior DJ** (2023) Cool ice with hot properties. *Nature Geoscience* **16**(12), 1073.

865 **Faria SH, Weikusat I and Azuma N** (2014) The microstructure of polar ice. Part I: Highlights

866   from ice core research. *Journal of Structural Geology* **61**, 2–20.

867 **Faria SH, Freitag J and Kipfstuhl S** (2010) Polar ice structure and the integrity of ice-core

868   paleoclimate records. *Quaternary Science Reviews* **29**(1–2), 338–351.

869 **Fegyveresi JM, Alley RB, Voigt DE, Fitzpatrick JJ and Wilen LA** (2019) Instruments and

870   methods: a case study of ice core bubbles as strain indicators. *Annals of Glaciology*

871   **60**(78), 8–19.

872 **Flin F, Brzoska JB, Lesaffre B, Coléou C and Pieritz RA** (2004) Three-dimensional geometric

873   measurements of snow microstructural evolution under isothermal conditions. *Annals*

874   *of Glaciology* **38**, 39–44. doi:10.3189/172756404781814942.

875 **Gerber TA and others** (2023) Crystal orientation fabric anisotropy causes directional hardening

876   of the Northeast Greenland Ice Stream. *Nature Communications* **14**(1), 1–12.

877   doi:https://doi.org/10.1038/s41467-023-38139-8.

878 **Gillet-Chaulet F, Gagliardini O, Meyssonnier J, Montagnat M and Castelnau O** (2005) A user-

879   friendly anisotropic flow law for ice-sheet modeling. *Journal of Glaciology* **51**(172), 3–14.

880   doi:10.3189/172756505781829584.

881 **Gow AJ and Williamson T** (1976) Rheological implications of the internal structure and crystal

882   fabrics of the West Antarctic ice sheet as revealed by deep core drilling at Byrd Station.

883   *GSA Bulletin* **87**(12), 1665–1677.

884 **Granger R, Flin F, Ludwig W, Hammad I and Geindreau C** (2021) Orientation selective grain

885   sublimation-deposition in snow under temperature gradient metamorphism observed

886   with diffraction contrast tomography. *Cryosphere* **15**(9), 4381–4398. doi:10.5194/TC-15-

887   4381-2021.

888   **Heggli M and others** (2011) Measuring snow in 3-D using X-ray tomography: assessment of

889   visualization techniques. *Annals of Glaciology* **52**(58), 231–236.

890   doi:10.3189/172756411797252202.

891   **Jia K, Baker I, Liu F and Dudley M** (1996) Observation of slip transmission through a grain

892   boundary in ice. *Journal of Materials Science* **31**(9), 2373–2378.

893   doi:10.1007/BF01152949.

894   **Journaux B and others** (2019) Recrystallization processes, microstructure and crystallographic

895   preferred orientation evolution in polycrystalline ice during high-temperature simple

896   shear. *Cryosphere* **13**(5), 1495–1511. doi:10.5194/TC-13-1495-2019.

897   **Kaempfer TU and Schneebeli M** (2007) Observation of isothermal metamorphism of new snow

898   and interpretation as a sintering process. *Journal of Geophysical Research: Atmospheres*

899   **112**(D24), 24101. doi:10.1029/2007JD009047.

900   **Kamb WB** (1961) The Glide Direction in Ice. *Journal of Glaciology* **3**(30), 1097–1106.

901   doi:10.3189/S0022143000017500.

902   **Kipfstuhl S and others** (2009) Evidence of dynamic recrystallization in polar firn. *Journal of*

903   *Geophysical Research: Solid Earth* **114**(B5), 5204. doi:10.1029/2008JB005583.

904   **Kipfstuhl S and others** (2006) Microstructure mapping: a new method for imaging deformation-

905   induced microstructural features of ice on the grain scale. *Journal of Glaciology* **52**(178),

906   398–406. doi:10.3189/172756506781828647.

907   **Kipfstuhl S, Pauer F, Kuhs WF and Shoji H** (2001) Air bubbles and clathrate hydrates in the

908   transition zone of the NGRIP deep ice core. *Geophysical Research Letters* **28**(4), 591–

909   594.

910   **Kuiper EJN, Weikusat I, De Bresser JHP, Jansen D, Pennock GM and Drury MR** (2020) Using a

911   composite flow law to model deformation in the NEEM deep ice core, Greenland - Part

912   1: The role of grain size and grain size distribution on deformation of the upper 2207 m.

913   *Cryosphere* **14**(7), 2429–2448. doi:10.5194/TC-14-2429-2020.

914   **De La Chapelle S, Castelnau O, Lipenkov V and Duval P** (1998) Dynamic recrystallization and

915   texture development in ice as revealed by the study of deep ice cores in Antarctica and

916   Greenland. *Journal of Geophysical Research: Solid Earth* **103**(B3), 5091–5105.

917   **Langway C** (1958) *Ice fabrics and the universal stage.* Department of the Army, Corps of

918   Engineers, Snow Ice and Permafrost Research Establishment.

919   **Lauritzen ML and others** (2024) Modeled Greenland Ice Sheet evolution constrained by ice-

920   core-derived Holocene elevation histories. *Preprint*. doi:10.5194/EGUSPHERE-2024-

921   2223.

922   **Lilien DA and others** (2023) Simulating higher-order fabric structure in a coupled, anisotropic

923   ice-flow model: application to Dome C. *Journal of Glaciology* **69**(278), 2007–2026.

924   doi:10.1017/JOG.2023.78.

925   **Liu F, Baker I and Dudley M** (1995) Dislocation-grain boundary interactions in ice crystals.

926   *Philosophical Magazine A* **71**(1), 15–42. doi:10.1080/01418619508242954.

927   **Liu F, Baker I, Yao G and Dudley M** (1992) Dislocations and grain boundaries in polycrystalline

928   ice: a preliminary study by synchrotron X-ray topography. *Journal of Materials Science*

929   **27**(10), 2719–2725. doi:10.1007/BF00540695.

930   **Mangler MF, Humphreys MCS, Wadsworth FB, Iveson AA and Higgins MD** (2022) Variation of

931   plagioclase shape with size in intermediate magmas: a window into incipient plagioclase

932   crystallisation. *Contributions to Mineralogy and Petrology* **177**(6), 1–21.

933   doi:10.1007/S00410-022-01922-9.

934   **Matsuda M** (1979) Determination of a-Axis Orientations of Polycrystalline Ice. *Journal of*

935   *Glaciology* **22**(86), 165–169. doi:10.3189/S0022143000014143.

936   **Miyamoto A, Weikusat I and Hondoh T** (2011) Complete determination of ice crystal

937   orientation using Laue X-ray diffraction method. *Journal of Glaciology* **57**(201), 103–110.

938   doi:10.3189/002214311795306754.

939   **Mojtabavi S and others** (2020) A first chronology for the East Greenland Ice-core Project

940   (EGRIP) over the Holocene and last glacial termination. *Climate of the Past* **16**(6), 2359–

941   2380. doi:10.5194/CP-16-2359-2020.

942   **Montagnat M, Chauve T, Barou F, Tommasi A, Beausir B and Fressengeas C** (2015) Analysis of

943   dynamic recrystallization of ice from EBSD orientation mapping. *Frontiers in Earth*

944   *Sciences* **3**, 1–13. doi:10.3389/FEART.2015.00081.

945   **Montagnat M and others** (2014) Multiscale modeling of ice deformation behavior. *Journal of*

946   *Structural Geology* **61**, 78–108. doi:10.1016/J.JSG.2013.05.002.

947   **Montagnat M and others** (2014) Fabric along the NEEM ice core, Greenland, and its

948   comparison with GRIP and NGRIP ice cores. *The Cryosphere* **8**, 1129–1138.

949   doi:10.5194/tc-8-1129-2014.

950   **Monz ME and others** (2021) Full crystallographic orientation (c and a axes) of warm, coarse-

951   grained ice in a shear-dominated setting: A case study, Storglaciären, Sweden.

952   *Cryosphere* **15**(1), 303–324. doi:10.5194/TC-15-303-2021.

953   **Morgan DJ and Jerram DA** (2006) On estimating crystal shape for crystal size distribution

954   analysis. *Journal of Volcanology and Geothermal Research* **154**(1–2), 1–7.

955   doi:10.1016/J.JVOLGEORES.2005.09.016.

956   **Musy M and others** (2025) vedo, a python module for scientific analysis and visualization of 3D

957   objects and point clouds, marcomusy/vedo: v2025.5.3. *Zenodo*.

958   doi:10.5281/ZENODO.14772685.

959   **NEEM community members** (2013) Eemian interglacial reconstructed from a Greenland folded

960   ice core. *Nature* **493**(7433), 489–494.

961   **Oddershede J, Bachmann F, Sun J and Lauridsen E** (2022) Advanced Acquisition Strategies for

962   Lab - Based Diffraction Contrast Tomography. *Integrating Materials and Manufacturing*

963   *Innovation* **11**, 1–12. doi:10.1007/s40192-021-00249-w.

964   **Pauer F, Kipfstuhl J and Kuhs WF** (1996) Raman spectroscopic study on the spatial distribution

965   of nitrogen and oxygen in natural ice clathrates and their decomposition to air bubbles.

966   *Geophysical Research Letters* **23**(2), 177–180. doi:10.1029/95GL03660.

967   **Placidi L, Greve R, Seddik H and Faria SH** (2010) Continuum-mechanical, Anisotropic Flow

968   model for polar ice masses, based on an anisotropic Flow Enhancement factor.

969   *Continuum Mechanics and Thermodynamics* **22**(3), 221–237. doi:10.1007/S00161-009-

970   0126-0.

971   **Prior DJ and others** (2015) Making EBSD on water ice routine. *Journal of Microscopy* **259**(3),

972   237–256.

973   **Prior DJ and others** (1999) The application of electron backscatter diffraction and orientation

974   contrast imaging in the SEM to textural problems in rocks. *American Mineralogist*

975   **84**(11–12), 1741–1759.

976   **Qi C and others** (2019) Crystallographic preferred orientations of ice deformed in direct-shear

977   experiments at low temperatures. *Cryosphere* **13**(1), 351–371. doi:10.5194/TC-13-351-

978   2019.

979   **Ranganathan M, Minchew B, Meyer CR and Peč M** (2021) Recrystallization of ice enhances the

980   creep and vulnerability to fracture of ice shelves. *Earth and Planetary Science Letters*

981   **576**, 117219. doi:10.1016/J.EPSL.2021.117219.

982   **Ranganathan M and Minchew B** (2024) A modified viscous flow law for natural glacier ice:

983   Scaling from laboratories to ice sheets. *Proceedings of the National Academy of Sciences*

984   *of the United States of America* **121**(23), e2309788121.

985   **Rasmussen SO and others** (2013) A first chronology for the North Greenland Eemian Ice Drilling

986   (NEEM) ice core. *Climate of the Past* **9**(6), 2713–2730. doi:10.5194/CP-9-2713-2013.

987   **Richards DHM, Pegler SS, Piazolo S and Harlen OG** (2021) The evolution of ice fabrics: A

988   continuum modelling approach validated against laboratory experiments. *Earth and*

989   *Planetary Science Letters* **556**, 116718. doi:10.1016/J.EPSL.2020.116718.

990   **Riche F, Montagnat M and Schneebeli M** (2013) Evolution of crystal orientation in snow during

991   temperature gradient metamorphism. *Journal of Glaciology* **59**(213), 47–55.

992   doi:10.3189/2013JOG12J116.

993   **Rigsby GP** (1951) Crystal Fabric Studies on Emmons Glacier Mount Rainier, Washington. *The*

994   *Journal of Geology* **59**(6), 590–598. doi:10.1086/625914.

995   **Roessiger J, Bons PD and Faria SH** (2014) Influence of bubbles on grain growth in ice. *Journal of*

996   *Structural Geology* **61**, 123–132. doi:10.1016/J.JSG.2012.11.003.

997   **Rolland du Roscoat S and others** (2011) Analysis of Snow Microstructure by Means of X-Ray

998   Diffraction Contrast Tomography. *Advanced Engineering Materials* **13**(3), 128–135.

999   doi:10.1002/ADEM.201000221.

1000 **Rollett A, Rohrer GS and Humphreys J** (2017) *Recrystallization and Related Annealing*

1001   *Phenomena.*, 3rd edn. Elsevier, Oxford. doi:10.1016/j.matchar.2020.110382.

1002 **Russell-Head D and Wilson C** (2001) Automated fabric analyser system for quartz and ice. *In*

1003   *Geological Society of Australia Abstracts* **64**(159).

1004 **Schneebeli M and Sokratov SA** (2004) Tomography of temperature gradient metamorphism of

1005   snow and associated changes in heat conductivity. *Hydrological Processes* **18**(18), 3655–

1006   3665.

1007 **Seierstad IK and others** (2014) Consistently dated records from the Greenland GRIP, GISP2 and

1008   NGRIP ice cores for the past 104 ka reveal regional millennial-scale δ18O gradients with

1009   possible Heinrich event imprint. *Quaternary Science Reviews* **106**, 29–46.

1010   doi:10.1016/J.QUASCIREV.2014.10.032.

1011 **Shoji H and Langway CC** (1985) Mechanical Properties of Fresh Ice Core from Dye 3, Greenland.

1012   *Greenland Ice Core: Geophysics, Geochemistry, and the Environment* **33**, 39–48.

1013   doi:10.1029/GM033P0039.

1014 **Shoji H and Langway CC** (1983) Volume relaxation of air inclusions in a fresh ice core. *Journal of*

1015   *Physical Chemistry* **87**(21), 4111–4114.

1016 **Stoll N and others** (2024) EastGRIP ice core reveals the exceptional evolution of crystallographic

1017   preferred orientation throughout the Northeast Greenland Ice Stream. *Preprint*.

1018   doi:10.5194/EGUSPHERE-2024-2653.

1019 **Sun J, Bachmann F, Oddershede J and Lauridsen E** (2022) Recent advances of lab-based

1020   diffraction contrast tomography – reconstruction speed benchmark testing and

1021   validations. *IOP Conference Series: Materials Science and Engineering* **1249**(1), 012045.

1022   doi:10.1088/1757-899X/1249/1/012045.

1023 **Svensson A and others** (2003) Properties of ice crystals in NorthGRIP late- to middle-Holocene

1024   ice. *Annals of Glaciology* **37**, 113–118. doi:10.3189/172756403781815636.

1025 **Svensson A, Baadsager P, Persson A, Hvidberg CS and Siggaard-Andersen ML** (2003) Seasonal

1026   variability in ice crystal properties at NorthGRIP: a case study around 301 m depth.

1027   *Annals of Glaciology* **37**, 119–122. doi:10.3189/172756403781815582.

1028   **Thorsteinsson T, Kipfstuhl J and Miller H** (1997) Textures and fabrics in the GRIP ice core.

1029   *Journal of Geophysical Research: Oceans* **102**(C12), 26583–26599.

1030   doi:10.1029/97JC00161.

1031   **Vallelonga P and others** (2014) Initial results from geophysical surveys and shallow coring of

1032   the Northeast Greenland Ice Stream (NEGIS). *Cryosphere* **8**(4), 1275–1287.

1033   doi:10.5194/TC-8-1275-2014.

1034   **Weikusat I and others** (2017) Physical analysis of an Antarctic ice core—towards an integration

1035   of micro- and macrodynamics of polar ice*. *Philosophical Transactions of the Royal

1036   Society A: Mathematical, Physical and Engineering Sciences* **375**(2086).

1037   doi:10.1098/RSTA.2015.0347.

1038   **Weikusat I, de Winter DAM, Pennock GM, Hayles M, Schneijdenberg CTWM and Drury MR**

1039   (2011) Cryogenic EBSD on ice: Preserving a stable surface in a low pressure SEM. *Journal

1040   of Microscopy* **242**(3), 295–310.

1041   **Weikusat I, Miyamoto A, Faria SH, Kipfstuhl S, Azuma N and Hondoh T** (2011) Subgrain

1042   boundaries in Antarctic ice quantified by X-ray Laue diffraction. *Journal of Glaciology*

1043   **57**(201), 111–120. doi:10.3189/002214311795306628.

1044   **Westhoff J and others** (2024) Combining traditional and novel techniques to increase our

1045   understanding of the lock-in depth of atmospheric gases in polar ice cores – results from

1046   the EastGRIP region. *The Cryosphere* **18**(9), 4379–4397. doi:10.5194/TC-18-4379-2024.

1047   **Westhoff J and others** (2021) A stratigraphy-based method for reconstructing ice core

1048   orientation. *Annals of Glaciology* **62**(85–86), 191–202. doi:10.1017/AOG.2020.76.

1049   **Wilen LA, Diprinzio CL, Alley RB and Azuma N** (2003) Development, principles, and applications

1050   of automated ice fabric analyzers. *Microscopy Research and Technique* **62**(1), 2–18.

1051   **Wilson CJL, Peternell M, Piazolo S and Luzin V** (2014) Microstructure and fabric development in

1052   ice: Lessons learned from in situ experiments and implications for understanding rock

1053   evolution. *Journal of Structural Geology* **61**, 50–77. doi:10.1016/J.JSG.2013.05.006.

1054   **Wilson CJL, Russell-Head DS and Sim HM** (2003) The application of an automated fabric

1055   analyzer system to the textural evolution of folded ice layers in shear zones. *Annals of

1056   Glaciology* **37**, 7–17. doi:10.3189/172756403781815401.

1057   **Winkelmann A, Jablon BM, Tong VS, Trager-Cowan C and Mingard KP** (2020) Improving EBSD

1058   precision by orientation refinement with full pattern matching. *Journal of Microscopy*

1059   **277**(2), 79–92. doi:https://doi.org/10.1111/jmi.12870.

1060   **Zhang Y and others** (2024) Formation Mechanisms of Large-Scale Folding in Greenland's Ice

1061   Sheet. *Geophysical Research Letters* **51**(16), e2024GL109492.

1062   doi:10.1029/2024GL109492.

1063

1064 **Mapping textures of polar ice cores using 3D laboratory X-ray microscopy**

1065

1066 Olivia A. Barbee[1,2], Jette Oddershede[1], Ravi Raj Purohit Purushottam Raj Purohit[1], Håkon W.

1067 Ånes[1], Jonas Engqvist[2], Anders Svensson[3], Nicholas M. Rathmann[3], Thomas Blunier[3], Florian

1068 Bachmann[1], and Stephen Hall[2]

1069

1070 **SUPPLEMENTARY MATERIAL**
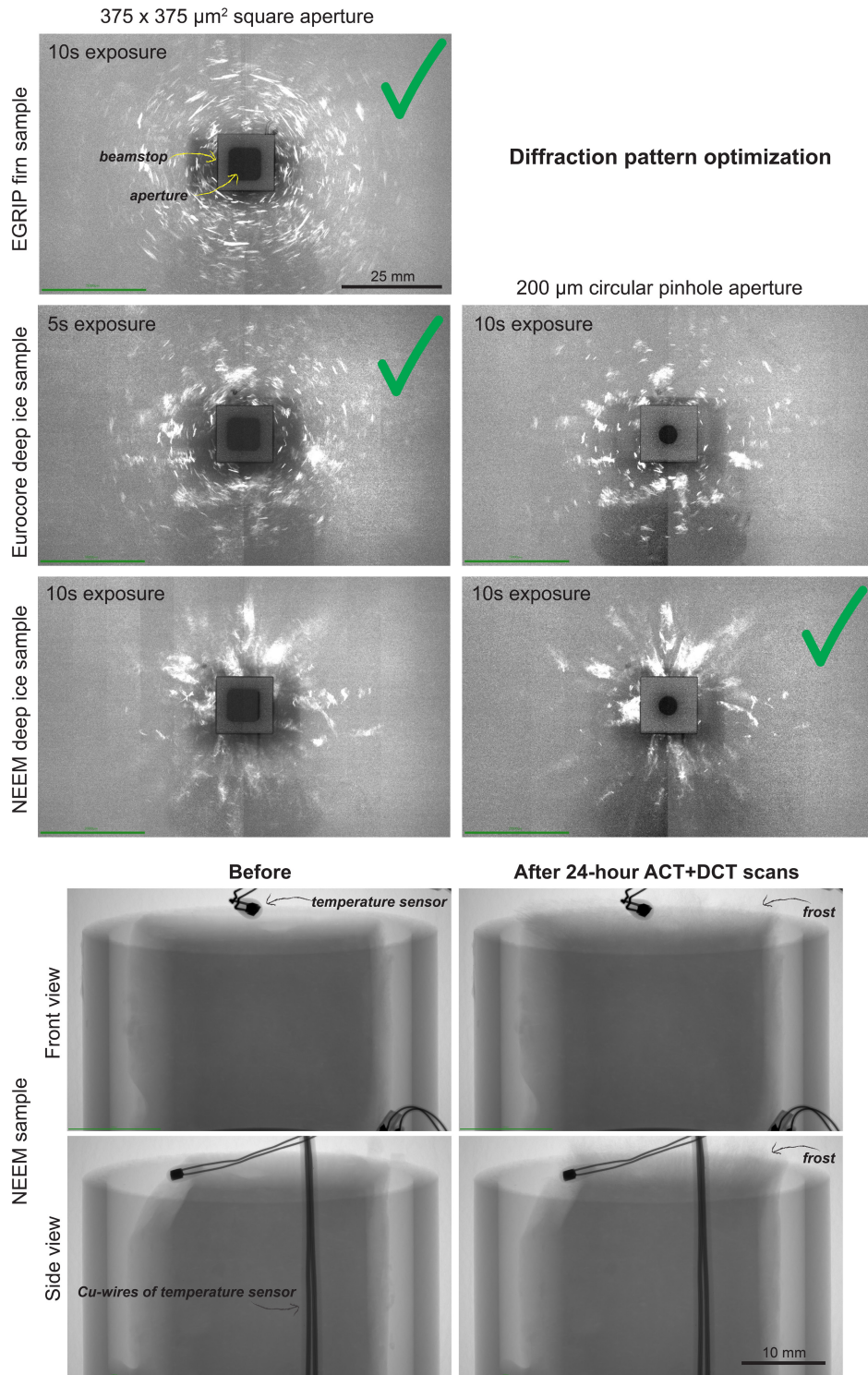
Figure S1. Examples of X-ray projections. At the top, raw X-ray diffraction projections show how the source-beam aperture affects the shapes of diffraction spots when using the beam geometry and flat panel detector as described in the **Methods**. The checkmarks indicate what aperture and exposure time proved optimal for DCT data acquisition on samples with different amounts of deformation. The radiographs of the NEEM sample show its appearance before and after a 24-hour-long period of ACT-

1077   DCT data acquisition. The only notable difference in the "after" image is the presence of a frost layer on

1078   the upper surface of the sample. The uppermost temperature sensor and its copper wires are in the

1079   field of view here; the wires had negligible effects on diffraction projections.
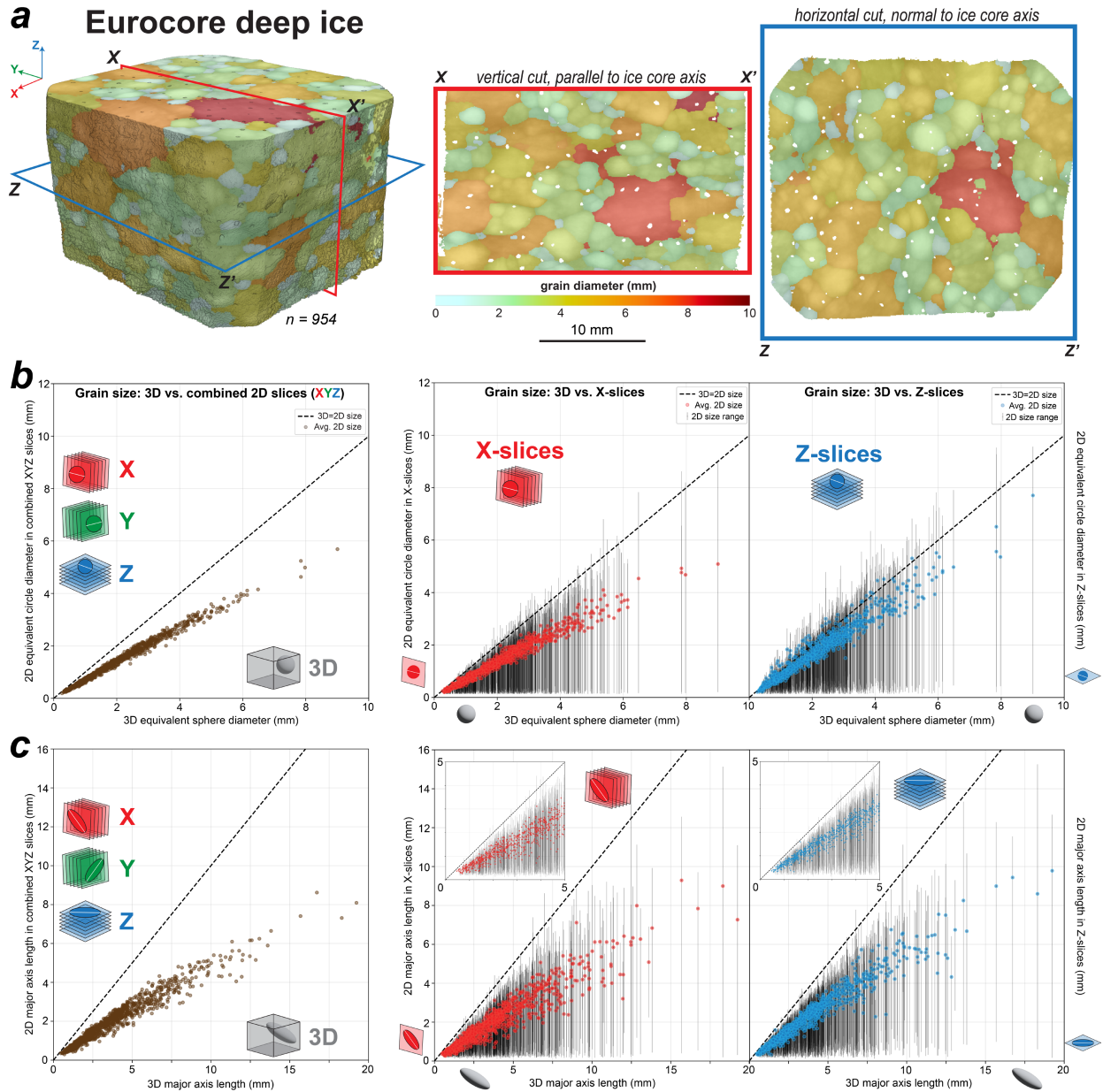
1080

Figure S2. Comparing grain size information between 3D grain maps and simulated 2D slices of the Eurocore deep ice sample. **(a)** The 3D grain map, colored by grain diameter, was sliced orthogonally. X and Z slices simulate the typical vertical (X) and horizontal (Z) cuts made of ice cores. **(b-c)** Multiple XYZ slices in these plots represent 60 μm intervals (i.e., the reconstructed voxel size of DCT data). Grain sizes calculated from 3D volumetric data are plotted against grain sizes calculated from combined XYZ orthogonal slices, hence the 1:1 line, as well as the average 2D size of each grain found across XYZ slices combined. Each grain's average size based on either all X-slices or all Z-slices is also compared to its volume-calculated size, with the full 2D size range for each grain plotted as vertical bars. Note that **(b)** plots diameters represent equivalent sphere (3D) or circle (2D) diameters, whereas **(c)** plots the major-axis length of grains based on ellipsoid (3D) and ellipse (2D) fitting.
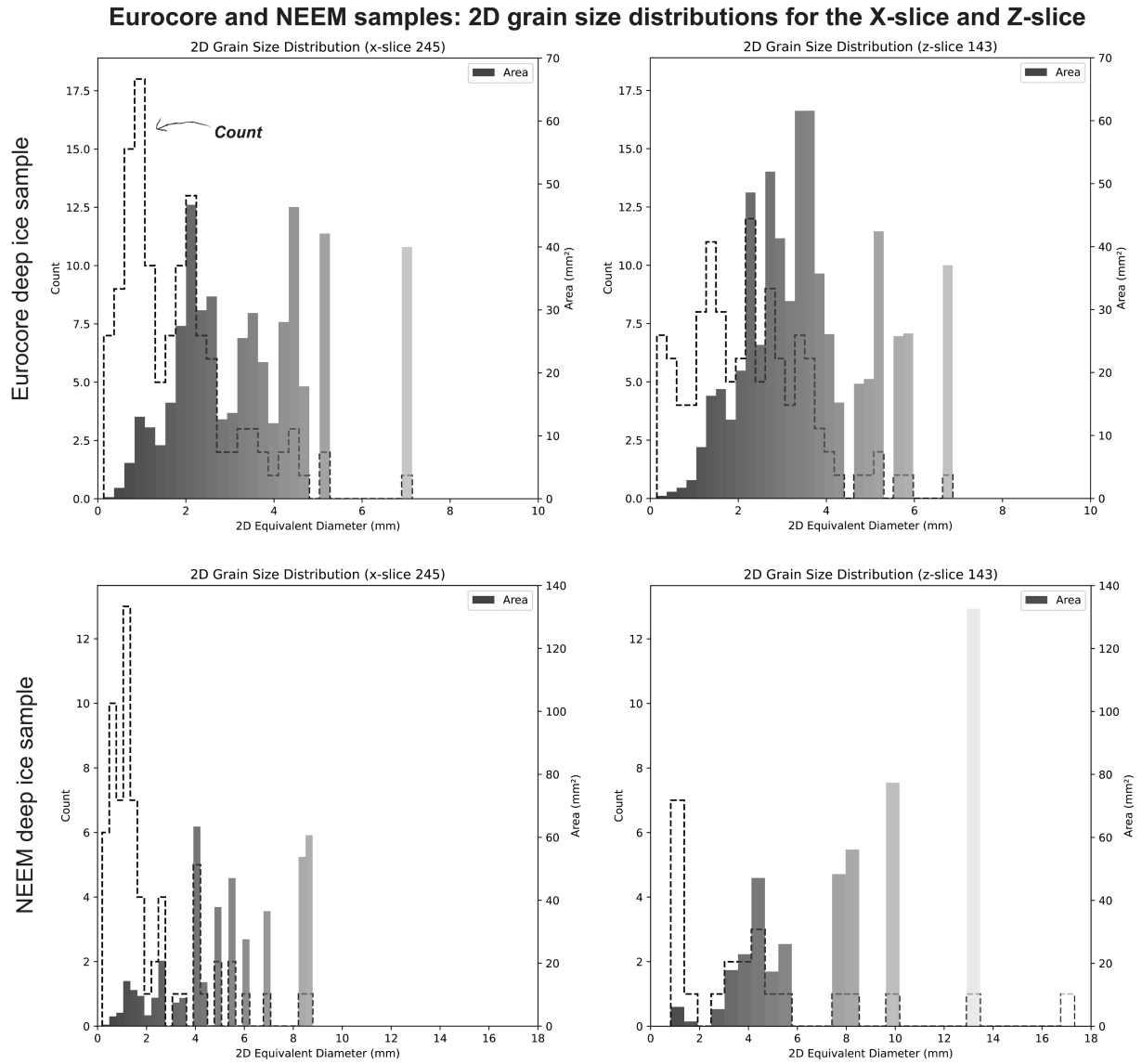
Eurocore and NEEM samples: 2D grain size distributions for the X-slice and Z-slice

1093
1094
1095 **Figure S3.** Grain size distributions for the single X-slice and Z-slice of the Eurocore and NEEM samples in
1096 **Figure 5** of the main text and **Figure S2**.
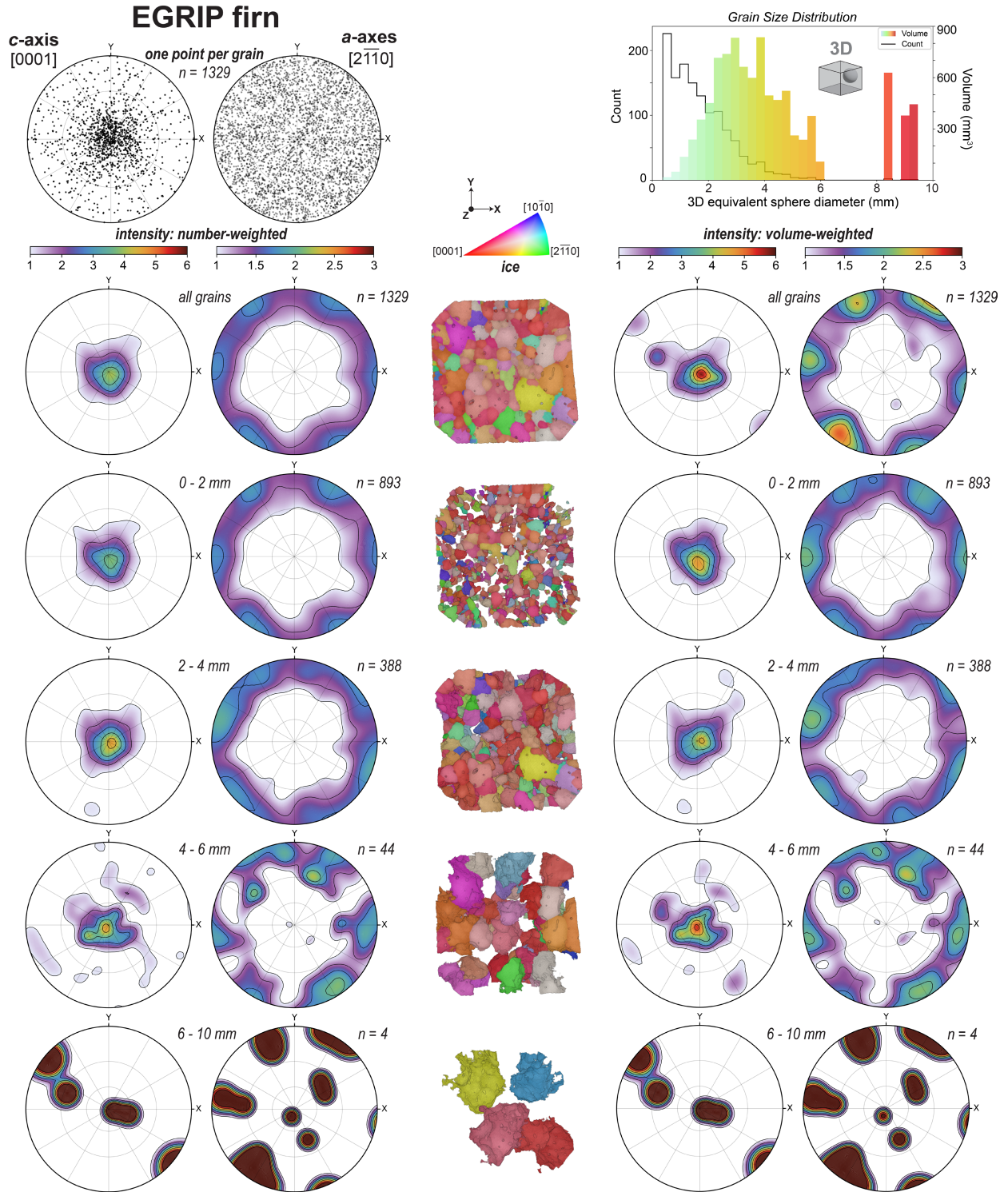
1097
1098
1099 **Figure S4.** Comparing pole figure analysis of firn grain orientations based upon count, volume, and grain
1100 size fraction. Pole figures provide views down the sample Z-axis, parallel to the ice-core axis. Analytical
1101 details are provided in the **Methods**. Note that glaciological studies employing EBSD of ice may instead

1102   represent the *a*-axes as $[11\bar{2}0]$ (-a$_3$), which is symmetrically equivalent to $[2\bar{1}\bar{1}0]$ (+a$_1$) (e.g., see Qi and
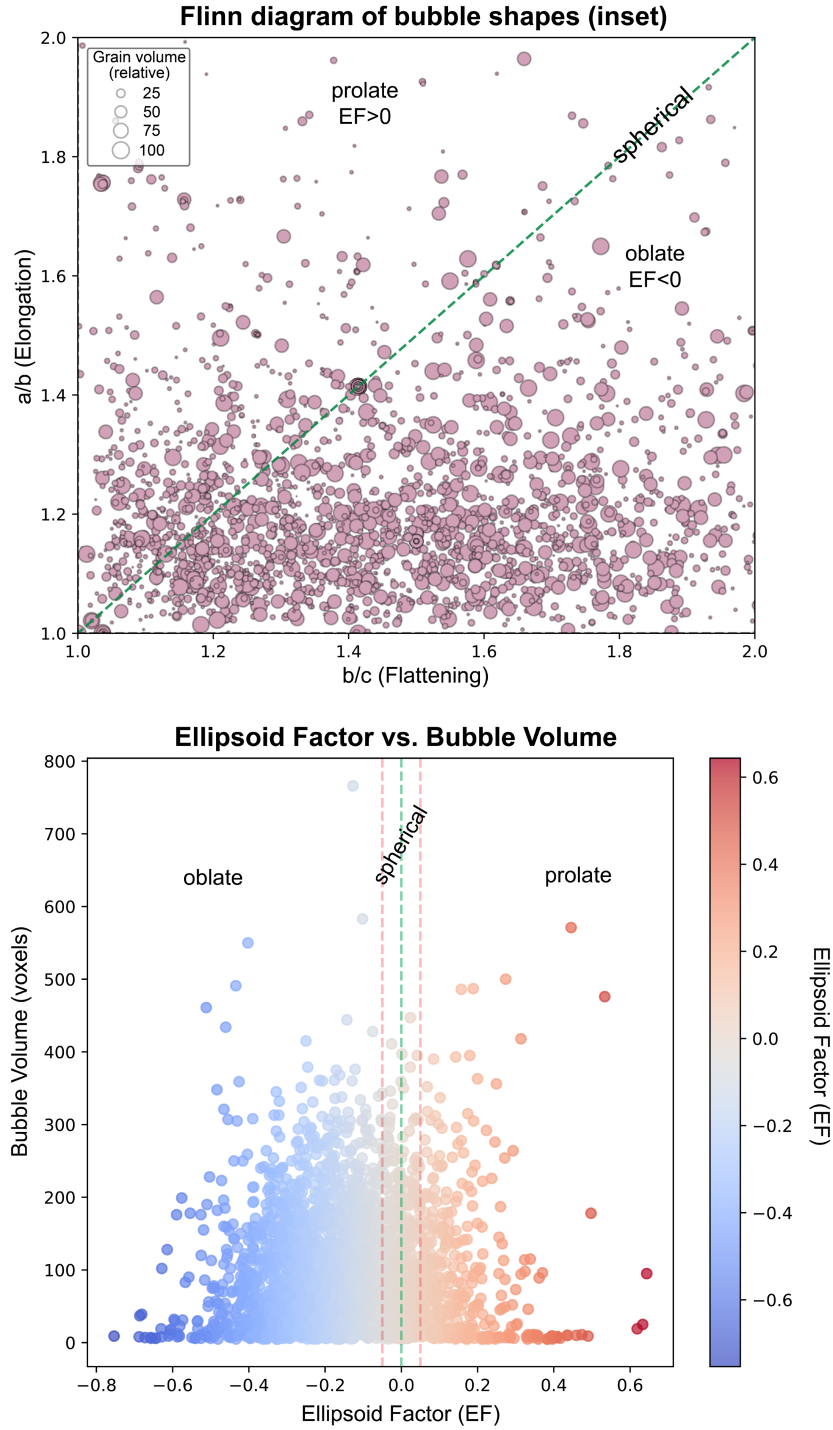1103   others, 2019).
1104

Figure S5. Additional analytical plots supporting observations reported in Section 3.5. The Flinn diagram for bubbles in the Eurocore sample represents an inset of the diagram included in **Figure 10** of the main text. The lower plot shows the distribution of the bubbles based on bubble volume and ellipsoid factor.
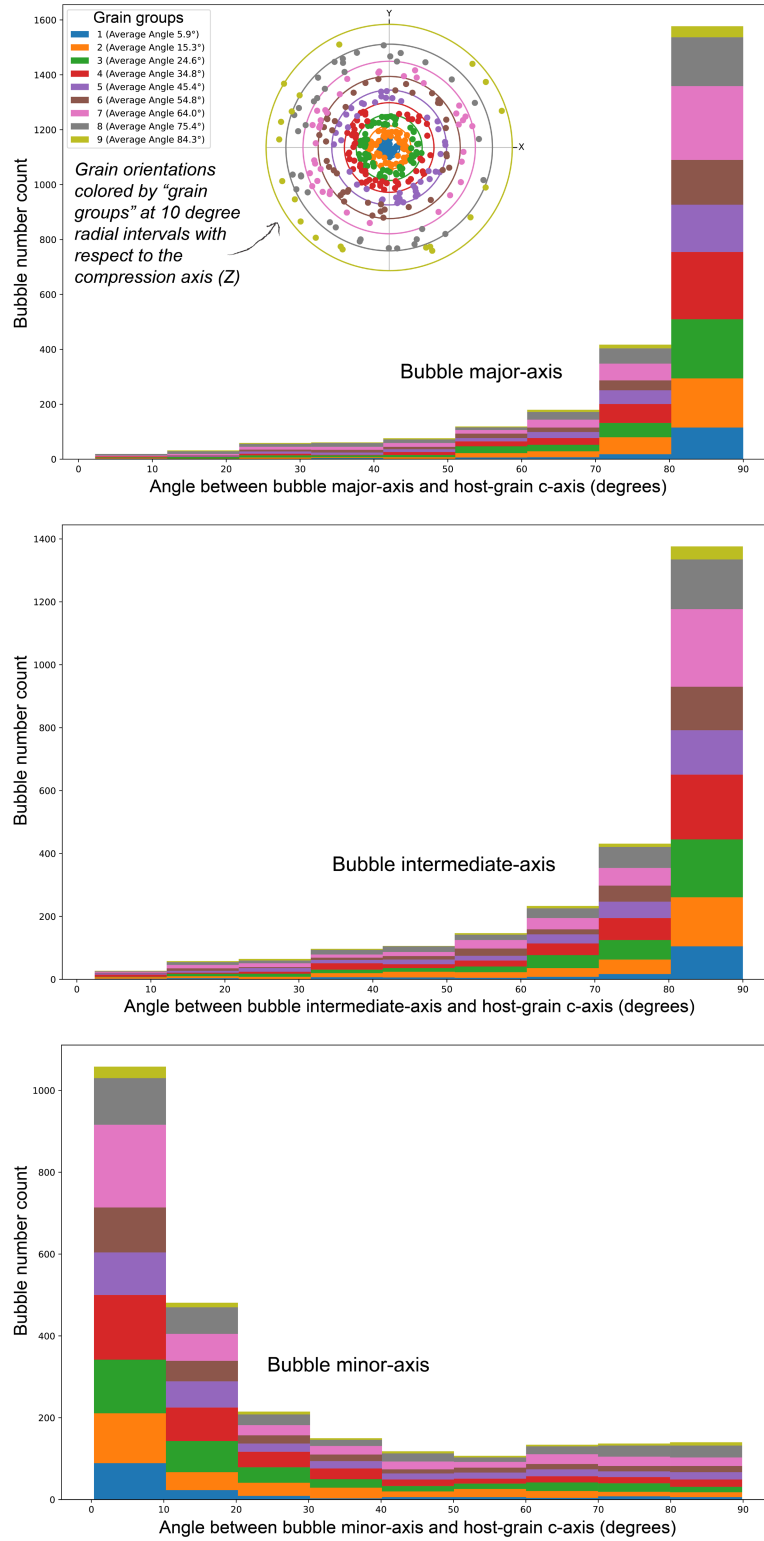
Bubbles in Eurocore deep ice: Stacked distribution of intragranular bubble-axis directions

1110
1111
1112 **Figure S6.** Stacked histograms showing the distribution of angle-differences between directions of
1113 bubble axes and the host-grain *c*-axis, with respect to how the host-grain *c*-axis is oriented relative to

1114   the compression axis (Z). The "grain groups" represent grains within 10-degree radial intervals away

1115   from the vertical (Z) direction, which represents the ice-core axis and direction of maximum

1116   compression. In the legend, the average *c*-axis angle misorientation from the Z-direction is reported for

1117   each "grain group".